







No Blue without Red: Evolutionary Properties of Super-Early Galaxies

A. FERRARA ¹, G. RODIGHIERO ², S. CARNIANI ¹, Z. ZHANG ^{1,3,4}, M. KOHANDEL ¹ AND B. DAS ¹

¹*Scuola Normale Superiore, Piazza dei Cavalieri 7, 50126 Pisa, Italy*

²*Dipartimento di Fisica e Astronomia "G. Galilei", Università di Padova, Vicolo dell'Osservatorio 3, 35131 Padova, Italy*

³*National Astronomical Observatories, Chinese Academy of Sciences, 20A Datun Road, Chaoyang District, Beijing 100101, P. R. China*

⁴*School of Astronomy and Space Science, University of Chinese Academy of Sciences, Beijing 100049, P. R. China*

(Revised May 25, 2026)

ABSTRACT

The discovery of numerous luminous, super-early galaxies at $z > 10$ by *JWST* has revealed a striking diversity in their ultraviolet (UV) properties, ranging from extremely blue, dust-poor systems to a smaller population of significantly reddened sources. We investigate the physical origin of this diversity within the framework of the Attenuation-Free Model (AFM), in which radiation-driven outflows redistribute dust to large galactic radii, reducing the effective attenuation. Applying the model to a sample of 32 spectroscopically confirmed super-early galaxies, we derive their key physical properties, including halo mass, star formation efficiency, metallicity, and outflow extent. We find that these systems reside in massive halos ($\log M/M_\odot \sim 10.7$) and exhibit moderate ($0.01 \lesssim \epsilon_* \lesssim 0.05$) star formation efficiencies, while frequently reaching super-Eddington conditions that trigger powerful outflows. Within this framework, we propose an evolutionary sequence in which galaxies transition from a dust-obscured “Red Monster” phase to a UV-bright “Blue Monster” phase as outflows clear their central regions. The recently confirmed red galaxy EGS-z11-R0 at $z = 11.45$ is naturally interpreted as a system observed during this obscured phase. Compact ($r_e \lesssim 150$ pc) sources are instead difficult to reconcile within AFM; we speculate that their emission is dominated by an AGN. Our results provide a unified interpretation of super-early galaxy properties and highlight the key role of radiation-driven outflows in shaping galaxy evolution at cosmic dawn. Future observations with *JWST* and ALMA will be essential to test these predictions and further constrain the nature of the earliest galaxies.

Keywords: galaxies: high-redshift, galaxies: evolution, galaxies: formation, black hole physics, stars: formation

1. INTRODUCTION

The first few hundred million years after the Big Bang represent a critical phase in galaxy formation, when the earliest stellar systems assembled, enriched their interstellar media with heavy elements, and contributed to cosmic reionization (for reviews see Somerville & Davé 2015; Dayal & Ferrara 2018). Since its commissioning, the James Webb Space Telescope (JWST) has revolutionized our view of this epoch, revealing a surprisingly abundant population of luminous galaxies at $z > 10$, corresponding to cosmic ages $\lesssim 500$ Myr (e.g., Naidu et al. 2022; Harikane et al. 2022; Castellano et al. 2023;

Bunker et al. 2023; Finkelstein et al. 2024; Curtis-Lake et al. 2023; Carniani et al. 2024; Naidu et al. 2025). A defining characteristic of the majority of these systems is their extremely blue rest-frame ultraviolet (UV) continuum slopes, often reaching $\beta_{UV} \lesssim -2.5$ (Morales et al. 2024; Cullen et al. 2024; Saxena et al. 2024; Austin et al. 2024; Dottorini et al. 2024). Such steep slopes are typically interpreted as evidence for young, metal-poor stellar populations with minimal dust attenuation, earning them the nickname “Blue Monsters” (Ferrara et al. 2023; Ziparo et al. 2023).

The properties of Blue Monsters – including their bright UV luminosities ($M_{UV} \lesssim -20$), compact sizes ($r_e \approx 200$ pc), and large stellar masses ($M_* \approx 10^9 M_\odot$) – have posed significant challenges to theoretical models based on pre-JWST expectations. In response, the

so-called “attenuation-free model” (AFM) has been proposed (Ferrara et al. 2023; Ziparo et al. 2023; Fiore et al. 2023; Ferrara 2024a,b). According to AFM, the extreme UV brightness and blue colors of these galaxies result from extremely low dust attenuation conditions, rather than from an intrinsic lack of dust. In this scenario, dust is produced by stars in standard net amounts but is subsequently pushed to kiloparsec scales by radiation-driven outflows, dramatically reducing the UV attenuation for a fixed dust mass (since $A_V \propto r^{-2}$). The AFM has successfully explained the shape of the UV luminosity functions at $z > 10$, the evolution of the cosmic star-formation rate density, and the star-formation histories of individual galaxies (Ferrara 2024a,b; Ferrara et al. 2025a).

A key prediction of the AFM is that the dust-to-stellar mass ratio ξ_d in Blue Monsters should be comparable to that measured in somewhat lower-redshift ($z \sim 7$) galaxies, i.e., $\log \xi_d \sim -2$ (Ferrara et al. 2022; Dayal et al. 2022; Sommovigo et al. 2022). However, direct observational constraints from JWST/NIRSpec spectra of 15 spectroscopically confirmed $z > 10$ galaxies instead indicate $\log \xi_d \lesssim -4$ (Ferrara et al. 2025c). This striking discrepancy suggests that standard dust production and destruction physics cannot reproduce the observed UV transparency of Blue Monsters. Within the AFM framework, this tension is resolved if dust is efficiently displaced from the central regions by radiation-driven outflows: while the total dust mass remains high, its redistribution to large radii significantly reduces the effective attenuation along the line of sight, yielding the observed UV transparency.

While super-early galaxy simulations show the presence of strong outflows (see e.g. Kohandel et al. 2025; Nakazato et al. 2024), direct observational evidence for such outflows in $z > 10$ galaxies has recently begun to emerge. Notably, deep JWST/NIRSpec observations of GS-z14-0 at $z = 14.18$, have revealed spatially offset CIII] $\lambda\lambda 1907, 1909$ emission extending up to ~ 400 pc from the stellar continuum, with a luminosity three times brighter than that measured in the nuclear spectrum (Carniani et al. 2026). The lack of a corresponding feature in ultra-deep NIRCам medium-band imaging implies that the emitting gas is diffuse rather than point-like, consistent with a scenario in which carbon-enriched gas has been expelled from the galaxy by ongoing or past outflows. From the CIII] luminosity, the authors derive a mass outflow rate of $M_{\text{out}} \approx 55 M_{\odot} \text{ yr}^{-1}$, corresponding to a mass-loading factor of $\eta = M_{\text{out}}/\text{SFR} \approx 1 - 5.5$. This suggests that outflows are highly efficient at early times, expelling gas at rates comparable to or exceeding then SFR.

Further support to the outflows scenario is provided by Tripodi et al. (2026) who presented a spatially resolved stacked analysis of 287 LAEs at $z > 4$ observed with JWST/NIRSpec prism spectroscopy. Similarly, Maiolino et al. (2024) in a study dedicate to GN-z11 ($z = 10.6$) find a deep, blue-shifted CIV $\lambda 1549$ absorption trough, tracing an outflow with a velocity of $\sim 800 \text{ km s}^{-1}$. The outflow is likely driven by radiation pressure from the combined stellar + AGN luminosity.

Further indirect evidence comes from the galaxy UNCOVER-37126 at $z \approx 10.25$. Marques-Chaves et al. (2026) find that this galaxy is undergoing an “ISM-naked” starburst phase, in which a strong outflow has cleared the remaining gas from its stellar core, allowing most LyC photons to escape.

Together, these observations provide support for the AFM framework, demonstrating that radiatively driven outflows are already operating at the earliest cosmic epochs, efficiently clearing dust and gas from the central regions of galaxies and thereby enabling the emergence of the bright, blue systems that JWST has revealed.

While the AFM provides a compelling framework for the dominant population of blue, dust-poor galaxies at $z > 10$, recent studies have uncovered a small but intriguing population of candidate (Rodighiero et al. 2023; Mitsunashi et al. 2025; Tang et al. 2025) or spectroscopically confirmed (Kokorev et al. 2025; Napolitano et al. 2025; Donnan et al. 2026; Rodighiero et al. 2026) high-redshift galaxies exhibiting significantly redder UV continua, i.e., $\beta_{\text{UV}} > -1.5$. These objects deviate markedly from the canonical $M_{\text{UV}}-\beta_{\text{UV}}$ relation established at $z \sim 6-9$ and extended to $z \sim 10-12$ with JWST. Their red slopes are difficult to reconcile with simple models of chemically primitive galaxies given the short age of the Universe at these epochs ($\lesssim 400$ Myr). Instead, significant dust attenuation ($A_V \sim 0.5-1$ mag, Kohandel et al. 2025) or extreme nebular continuum emission from dense, highly ionized gas have been proposed as possible explanations (Mitsunashi et al. 2025; Katz et al. 2025).

A landmark in this context is the recent spectroscopic confirmation of EGS-z11-R0 at $z = 11.452 \pm 0.021$ Rodighiero et al. (2026), the most distant red galaxy identified and confirmed to date. Discovered serendipitously through inspection of public JWST/NIRSpec data in the CEERS field, EGS-z11-R0 exhibits a remarkably flat UV continuum slope $\beta_{\text{UV}} \sim -1.0$, placing it well above the canonical $M_{\text{UV}}-\beta_{\text{UV}}$ relation at $z \sim 10-12$. The source shows significant detections of high-ionization UV emission lines such as CIV and CIII], and its spectral energy distribution (SED) requires substantial dust attenuation ($A_V \sim 1.2$ mag) and a stellar mass $\log(M_*/M_{\odot}) \sim 8.5-9.5$. While a moderate AGN

contribution cannot be excluded, the data robustly indicate a dust-enriched system observed during an early, possibly obscured phase of galaxy assembly.

The existence of such dust-reddened systems at $z > 10$ has important implications for our understanding of early chemical enrichment and galaxy evolution. Several theoretical models have explored the rapid buildup of galaxies at cosmic dawn. Ferrara (2024a) proposed that galaxies at $z > 10$ initially undergo a radiative feedback-regulated phase leading to bursty star formation. When dust shielding becomes important, the galaxy switches to a smooth, substantially obscured star formation regime—dubbed the “Red Monster” phase. During this obscured phase, which lasts $\simeq 20\%$ of the galaxy lifetime, $\simeq 70\%$ of the observed stars are formed. Eventually, as the galaxy becomes super-Eddington, a powerful radiation-driven outflow clears most of the dust, and the galaxy transitions into a “Blue Monster” dominating the bright end of the UV luminosity function. Other theoretical frameworks, such as the feedback-free model (Dekel et al. 2023; Li et al. 2023) or density-regulated star formation in semi-analytic models (Somerville et al. 2025), have also emphasized the possibility of rapid, early stellar mass assembly.

Observational evidence increasingly points toward rapid early stellar assembly at these epochs. Santini et al. (2025) showed that several $z > 10$ systems exhibit unexpectedly high stellar masses and specific star-formation rates, indicating that substantial stellar assembly had already occurred within the first few hundred million years. However, robust spectroscopic confirmation of strongly dust-reddened galaxies at $z > 10$ has until now been lacking. Most red candidates identified so far rely on broadband photometry, where degeneracies between dust, age, nebular emission, and AGN activity complicate the interpretation. The spectroscopic confirmation of EGS-z11-R0 thus provides a critical anchor for understanding whether chemically evolved, dust-enriched galaxies were already in place within the first ~ 400 Myr of cosmic history.

In this work, we investigate the origin of the observed diversity of super-early galaxies at $z > 10$ within the framework of the AFM. We apply the model to a sample of spectroscopically confirmed galaxies to derive their key physical properties – including halo mass, star formation efficiency, metallicity, and outflow extent – and to directly test the role of radiation-driven outflows in shaping their observable characteristics. We demonstrate that the coexistence of extremely blue and significantly reddened systems can be naturally explained as different stages of a common evolutionary sequence, in which galaxies transition from a dust-obscured phase to

a UV-bright one as outflows efficiently redistribute gas and dust. Within this unified framework, recently identified red systems, such as EGS-z11-R0, are interpreted as galaxies caught during an early, obscured phase of their evolution. This approach provides a physically motivated picture for the buildup of dust, metals, and stellar mass at cosmic dawn, and establishes a direct link between the observed properties of $z > 10$ galaxies and their underlying evolutionary pathways.

This paper is structured as follows. In Sec. 2 we outline the AFM and its key physical ingredients. In Sec. 3 we apply the model to a sample of spectroscopically confirmed $z > 10$ galaxies and derive their physical properties. We also interpret the results in terms of a unified evolutionary scenario linking dust-obscured and UV-bright phases. In Sec. 4 we discuss the nature of the compact galaxy subset and the possible role of AGN. Finally, Sec. 5 summarizes our conclusions. We adopt a Λ CDM cosmological model¹, and a Salpeter $1 - 100 M_{\odot}$ initial mass function.

2. ATTENUATION-FREE MODEL

The Attenuation-Free Model (AFM, Ferrara et al. 2023) provides a comprehensive framework to interpret the properties of super-early ($z > 10$) galaxies, and test and explore their implications. In addition to reproduce the observed UV luminosity functions and evolution of the cosmic star formation rate density (Ferrara 2024a), AFM also makes testable predictions on the galaxy dust content (Ferrara et al. 2025c), sub-mm observability (Ferrara et al. 2025a), escape fraction of Lyman continuum (Ferrara et al. 2025b) and Ly α (Ferrara 2024a) photons. Furthermore, it has been used to successfully derive the star formation history of super-early galaxies, like e.g. GS-z14-0 (Ferrara 2024b).

With the aim of understanding the origin of super-early galaxies diversity, and in particular their brightness and spectral colors, we apply AFM to the spectroscopically confirmed sources at $z > 10$. In the following we recall the AFM main features and key equations.

2.1. Galaxy sizes

We start by deriving the half-light (or effective) galaxy radius, r_e , under the standard assumption that the specific angular momentum of the halo is conserved during

¹ Throughout the paper, we assume a flat Universe with the following cosmological parameters: $\Omega_m = 0.3075$, $\Omega_{\Lambda} = 1 - \Omega_m$, and $\Omega_b = 0.0486$, $h = 0.6774$, $\sigma_8 = 0.826$, where Ω_m , Ω_{Λ} , and Ω_b are the total matter, vacuum, and baryon densities, in units of the critical density; h is the Hubble constant in units of $100 \text{ km s}^{-1} \text{ Mpc}^{-1}$, and σ_8 is the late-time fluctuation amplitude parameter (Planck Collaboration et al. 2014).

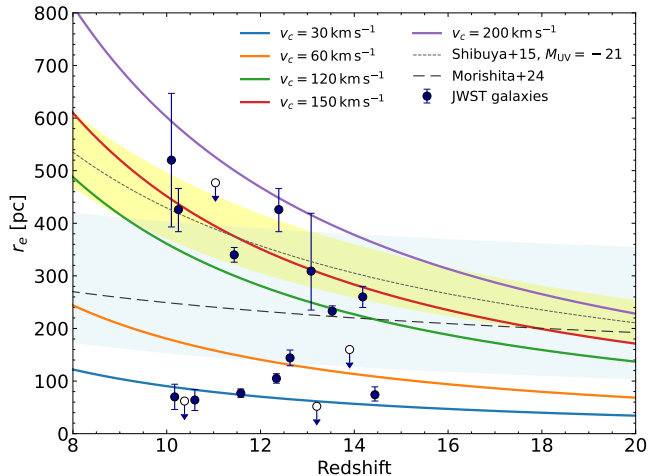


Figure 1. Predicted redshift evolution of the effective galaxy radius, r_e (eq. 1), for different values of the halo circular velocities, v_c , as shown by the legend. The data points represent our super-early galaxy sample presented in Tab. 1 along with the references. Open points indicate upper limits. Also shown are the best-fit curves and 1σ errors (shaded region) to high- z galaxy data from Shibuya et al. (2015) and Morishita et al. (2024).

disk formation (Mo et al. 2010). Hence, r_e is related to the halo virial radius, r_{vir} , via the spin parameter, λ , as

$$r_e = 1.678 \frac{\lambda}{\sqrt{2}} r_{\text{vir}} = 0.1678 \frac{\lambda}{\sqrt{2}} \frac{v_c}{H(z)}, \quad (1)$$

where v_c is the halo circular velocity. The numerical prefactor comes from the implicit assumption of an exponential disk, for which the effective radius is $r_e = 1.678$ times the disk scale-length. As shown by numerical simulations (Angel et al. 2016), λ depends very weakly on halo mass M and redshift. Its distribution is approximately log-normal with mean value $\lambda = 0.035$ and $\sigma_{\log \lambda} \approx 0.22$ dex scatter (Mo et al. 2010; Semenov 2026).

In Fig. 1 we compare $r_e(v_c)$ from eq. 1 with the observed effective radii of the spectroscopically confirmed super-early galaxies taken from the literature. Also shown is the extrapolation of the size evolution obtained by Shibuya et al. (2015) for bright ($M_{\text{UV}} \simeq -21$) Lyman Break Galaxies, and the same relation obtained by Morishita et al. (2024) for 341 galaxies at $5 < z < 14$, with 109 having spectroscopic redshift measurements from the literature.

As already noted by Harikane et al. (2025), super-early galaxies seem to fall in two distinct categories featuring either extended or compact morphologies. The first group is consistent with both the Shibuya et al. (2015) extrapolation and with our model for $v_c \sim 200 \text{ km s}^{-1}$ galaxies, showing r_e values $\gtrsim 250$ pc. In the range $10 < z < 14$ such circular velocity corresponds to halo

masses of $\simeq 10^{11} M_\odot$. The second group includes galaxies with $r_e \lesssim 150$ pc, or $v_c < 80 \text{ km s}^{-1}$. We note that the Morishita et al. (2024) best-fit seems to run in between the two distributions.

The origin of this dual distribution is unclear. The sharp separation is hard to be reconciled with the smooth, log-normal distribution of spin parameters, or smaller ($\lesssim 8 \times 10^9 M_\odot$) halo masses given their generally comparable inferred stellar masses ($\approx 10^{8-9} M_\odot$, see Tab. 1). As we discuss in Sec. 4, the most plausible scenario for these compact galaxies is that their UV light is dominated by AGN activity, as indeed suggested for GN-z11, GHZ2 and GHZ9, based on the detection of high-ionization emission lines (Maiolino et al. 2024; Castellano et al. 2024; Naidu et al. 2025; Napolitano et al. 2025).

2.2. Star formation rate

In the AFM, the mean star formation rate (SFR) in a halo of total mass M at redshift z is

$$\text{SFR}(M, z) = \epsilon_\star(v_c) f_b \frac{M}{t_{\text{ff}}(z)}, \quad (2)$$

where ϵ_\star is the *instantaneous* star formation efficiency depending on the halo circular velocity, $v_c(M, z)$; $f_b = \Omega_b/\Omega_m = 0.158$. The gas free-fall time in halos, $t_{\text{ff}} = (4\pi G\rho)^{-1/2}$, can be conveniently written as $t_{\text{ff}} = \zeta H(z)^{-1}$, where $H(z)^{-1}$ is the Hubble time at z and $\zeta = 0.06$ (Ferrara 2024b).

Following Ferrara et al. (2023) we write the efficiency as

$$\epsilon_\star(v_c) = \epsilon_0 \frac{v_c^2}{v_c^2 + f_w v_s^2}, \quad (3)$$

where $f_w = 0.12$ is the outflow coupling constant with the gas, and $v_s = \sqrt{\nu E_0}$ is a characteristic velocity associated with the SN energy ($E_0 = 10^{51}$ erg) released per unit stellar mass formed. We adopt $1 - 100 M_\odot$ Salpeter IMF for which $\nu = (52.9 M_\odot)^{-1}$, and $v_s = 975 \text{ km s}^{-1}$. According to eq. 2, the efficiency grows with v_c^2 (or $M_{\text{vir}}^{2/3}$) at low masses and flattens to $\epsilon_0 = 0.09$ for circular velocities $v_c \gtrsim f_w^{1/2} v_s$.

The previous incarnation of AFM and its parameters successfully reproduces the UV LF up to $z \sim 14$, along with the cosmic star formation rate density (Ferrara 2024a) and UV slope evolution (Ferrara et al. 2025b) and other observed super-early galaxy properties (Ferrara 2024b; Ferrara et al. 2025c). In Fig. 2 we show a comparison of the predicted UV LF at $z = 11$ and $z = 12$ with the available data. AFM matches very well the data at both redshifts. Interestingly, the shape of the predicted UV LF is perfectly fit by a standard double-power law whose parameters are reported in

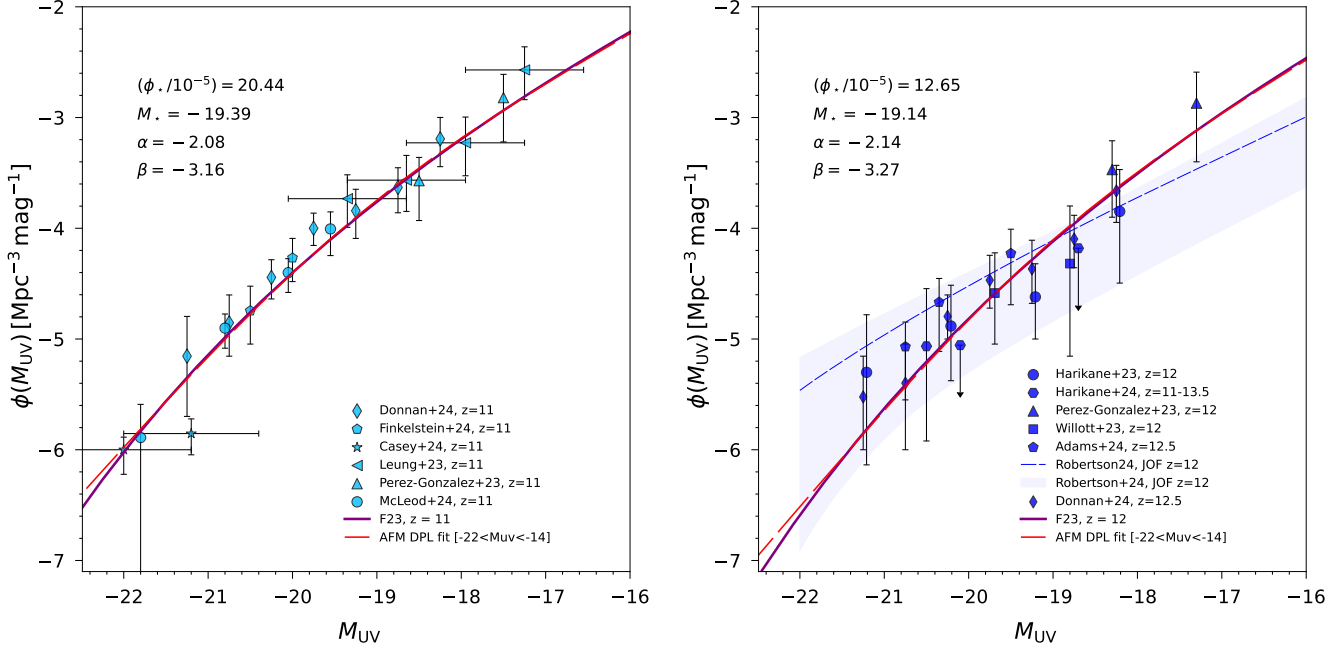


Figure 2. Attenuation-Free Model (AFM) predictions for the UV luminosity function at $z \simeq 11$ (left panel) and $z \simeq 12$ (right) compared to available JWST data. The model is well fitted by a double-power law (red curve) of the form $\phi(M_{UV}) = \phi_* [10^{(1+\alpha)x} + 10^{(1+\beta)x}]^{-1}$, where $x = -0.4(M_* - M_{UV})$, with parameters shown in the panels. Data points are taken from Donnan et al. (2024); Finkelstein et al. (2023); Casey et al. (2023); Leung et al. (2023); Pérez-González et al. (2023); McLeod et al. (2023); Harikane et al. (2023, 2024); Willott et al. (2024); Adams et al. (2024); Robertson et al. (2024)

the two panels. The faint-end slope at these epoch is rather steep, $\alpha \simeq -2.1$, when computed in the range $-22 < M_{UV} < -17$; we note that the slope is somewhat dependent on this choice. AFM also shows an excellent agreement to the cosmic star formation rate density data in the redshift range $5 < z < 15$. However, we note that some tension is appearing for $z \gtrsim 14$ where the data seem to indicate a slower decline. Moreover, if the photometric candidates (Pérez-González et al. 2025; Castellano et al. 2025) at $z \simeq 17$ and 25 are confirmed they would be extremely hard to reconcile not only with AFM but with essentially all Λ CDM-based galaxy evolution models. In that case one would be forced to introduce significant modifications, as e.g. PBH powering these sources (Matterì et al. 2025; Liu & Bromm 2023). Barring these uncertain data, we consider the agreement of the data with AFM as robust.

Using the observed values of r_e and SFR for each galaxy in the sample in combination with eqs. 1–2, we obtain² λ and v_c , which can be used to obtain the halo mass M , the corresponding amplitude of the fluctuation in units of the r.m.s. of the cosmological density field,

$\nu_\delta = \delta/\sigma$, the halo number density, n_M , and the star formation efficiency $\epsilon(v_c)$. These quantities are reported in Tab. 2.

2.3. Stellar mass

The stellar mass is obtained by integrating eq. 2,

$$M_*(t) = (1 - R) \int_{t_*}^t \epsilon_*(v_c) f_b \frac{M}{t_{\text{ff}}(z)} \left| \frac{dt}{dz} \right| dz. \quad (4)$$

where R is the gas return fraction of stars for the adopted IMF. Here we will make the simplifying assumption that most of the stars are formed in the last free-fall time, i.e. starting at $t_* = t - t_{\text{ff}}$, but we allow for slightly different durations via a order unity non-dimensional factor, Δ_{t_*} . Consistently, we redefine the stellar age as $\Delta_{t_*} t_{\text{ff}}$. At $z \simeq 10$, this implies a mass assembly of $\simeq 40$ Myr, which is consistent with the typical ages estimated through non-parametric star formation histories (Bouwens et al. 2022; Whitler et al. 2023; Donnan et al. 2024; López-Corredoira & Gutiérrez 2026).

Given such a short time lapse, we approximate the stellar mass as

$$M_*(M, z) \simeq (1 - R) \epsilon_*(v_c) f_b \Delta_{t_*} M; \quad (5)$$

it also follows that R is much smaller than in the commonly adopted case of Instantaneous Recycling Approximation (IRA), according to which stars with mass

² We account for errors on the free parameters of the model by sampling the experimental errors whose distribution is assumed to be gaussian.

Table 1. Observed properties of spectroscopically confirmed galaxies at $z > 10$. References are given in the legend.

Name	z	M_{UV}	β	SFR [M_{\odot}/yr]	$\log(M_*/M_{\odot})$	r_e [pc]	A_V	$\log(Z/Z_{\odot})$
EGS-25297 ¹	9.94	$-20.00^{+0.00}_{-0.00}$	$-1.51^{+0.08}_{-0.08}$	$117.00^{+21.00}_{-18.00}$	$8.95^{+0.04}_{-0.05}$	< 170	$0.92^{+0.42}_{-0.27}$	$-1.00^{+0.08}_{-0.08}$
UNCOVER-26185 ²	10.05	$-18.83^{+0.07}_{-0.07}$	$-2.29^{+6.00}_{-0.06}$	$1.70^{+0.40}_{-0.40}$	$8.23^{+0.07}_{-0.09}$	293^{+42}_{-42}	$0.20^{+0.09}_{-0.09}$	$-1.30^{+0.08}_{-0.09}$
CEERS2-7929 ³	10.10	$-19.30^{+0.00}_{-0.00}$	$-1.70^{+0.10}_{-0.10}$	$5.90^{+1.60}_{-2.60}$	$8.50^{+0.30}_{-0.40}$	520^{+127}_{-127}	$0.14^{+0.29}_{-0.14}$	–
MACS0647-JD2 ⁴	10.17	$-19.50^{+0.20}_{-0.20}$	$-2.60^{+0.10}_{-0.10}$	$2.40^{+1.00}_{-1.00}$	$7.50^{+0.10}_{-0.10}$	70^{+24}_{-24}	$0.01^{+0.00}_{-0.00}$	$-0.90^{+0.09}_{-0.09}$
UNCOVER-37126 ⁵	10.25	$-20.10^{+0.05}_{-0.05}$	$-2.88^{+0.10}_{-0.10}$	$9.60^{+4.60}_{-4.60}$	$7.77^{+0.06}_{-0.06}$	61^{+6}_{-6}	$0.03^{+0.03}_{-0.03}$	–
CAPERS-COS-109917 ⁶	10.27	$-19.57^{+0.11}_{-0.11}$	$-2.84^{+0.28}_{-0.28}$	$3.10^{+0.70}_{-0.80}$	$8.00^{+0.40}_{-0.30}$	–	$0.02^{+0.03}_{-0.01}$	$-0.90^{+0.20}_{-0.30}$
GS-z10-0 ⁷	10.38	$-18.61^{+0.10}_{-0.10}$	$-2.49^{+0.22}_{-0.22}$	$1.10^{+0.19}_{-0.16}$	$7.58^{+0.19}_{-0.20}$	< 62	$0.05^{+0.03}_{-0.02}$	$-1.91^{+0.25}_{-0.20}$
CAPERS_UDS_z10 ⁸	10.56	$-20.53^{+0.09}_{-0.09}$	$-2.27^{+0.12}_{-0.12}$	$18.00^{+5.00}_{-5.00}$	$8.30^{+0.20}_{-0.20}$	420^{+70}_{-70}	$0.31^{+0.10}_{-0.10}$	–
GN-z11 ⁹	10.60	$-21.50^{+0.02}_{-0.02}$	$-2.36^{+0.10}_{-0.10}$	$18.78^{+0.81}_{-0.69}$	$8.73^{+0.06}_{-0.06}$	64^{+20}_{-20}	$0.17^{+0.03}_{-0.03}$	$-0.92^{+0.06}_{-0.05}$
JADES-GS-20176151 ⁶	10.62	$-19.50^{+0.14}_{-0.14}$	$-2.11^{+0.17}_{-0.17}$	$2.70^{+0.80}_{-0.50}$	$8.10^{+0.10}_{-0.20}$	–	$0.02^{+0.06}_{-0.01}$	$-1.90^{+0.20}_{-0.20}$
EGS-22637 ¹⁰	10.70	$-20.23^{+0.12}_{-0.12}$	$-2.42^{+0.09}_{-0.09}$	$3.54^{+1.34}_{-0.98}$	$8.62^{+0.14}_{-0.14}$	524^{+134}_{-134}	$0.11^{+0.13}_{-0.13}$	$-1.69^{+0.40}_{-10.0}$
MoM-z11-2 ¹⁰	10.80	$-18.82^{+0.36}_{-0.36}$	$-1.60^{+0.22}_{-0.22}$	$2.69^{+1.02}_{-0.74}$	$8.58^{+0.18}_{-0.18}$	555^{+234}_{-234}	$0.13^{+0.10}_{-0.10}$	$-0.68^{+0.25}_{-0.62}$
CAPERS-EGS-43539 ¹⁰	10.82	$-18.82^{+0.36}_{-0.36}$	$-2.78^{+0.09}_{-0.09}$	$0.26^{+0.18}_{-0.11}$	$7.51^{+0.28}_{-0.28}$	< 61	$0.21^{+0.17}_{-0.17}$	$-1.52^{+0.30}_{-10.0}$
JADES-GS-20177294 ⁶	10.89	$-19.25^{+0.09}_{-0.09}$	$-2.34^{+0.55}_{-0.55}$	$0.30^{+0.60}_{-0.30}$	$8.10^{+0.20}_{-0.20}$	–	$0.07^{+0.11}_{-0.05}$	$-1.30^{+0.50}_{-0.50}$
MoM-z11-1 ¹⁰	10.92	$-19.98^{+0.24}_{-0.24}$	$-2.29^{+0.36}_{-0.36}$	$4.78^{+2.29}_{-1.55}$	$8.96^{+0.18}_{-0.18}$	636^{+235}_{-235}	$0.26^{+0.15}_{-0.15}$	$-1.52^{+0.60}_{-10.0}$
CAPERS_UDS_z11 ⁸	11.01	$-20.28^{+0.08}_{-0.08}$	$-1.71^{+0.12}_{-0.12}$	$43.00^{+10.00}_{-10.00}$	$8.70^{+0.20}_{-0.20}$	560^{+61}_{-61}	$0.74^{+0.11}_{-0.11}$	–
CEERS2-588 ¹¹	11.04	$-20.40^{+0.00}_{-0.00}$	$-1.74^{+0.25}_{-0.25}$	$8.20^{+0.00}_{-0.00}$	$9.05^{+0.07}_{-0.09}$	453^{+120}_{-82}	$0.12^{+0.10}_{-0.12}$	$-0.14^{+0.10}_{-0.13}$
JADES-GS-20015720 ⁶	11.27	$-19.56^{+0.17}_{-0.17}$	$-2.67^{+0.12}_{-0.12}$	$2.90^{+0.70}_{-1.00}$	$8.20^{+0.40}_{-0.30}$	–	$0.04^{+0.06}_{-0.03}$	$-1.50^{+0.40}_{-0.30}$
GS-z11-1 ¹²	11.25	$-19.40^{+0.08}_{-0.08}$	$-2.80^{+0.10}_{-0.10}$	$0.32^{+0.11}_{-0.11}$	$7.80^{+0.20}_{-0.20}$	73^{+10}_{-10}	$0.05^{+0.03}_{-0.02}$	$-1.55^{+0.12}_{-0.13}$
MAISIE ¹³	11.44	$-20.32^{+0.08}_{-0.06}$	$-2.47^{+0.09}_{-0.09}$	$2.10^{+4.80}_{-2.00}$	$8.50^{+0.29}_{-0.44}$	340^{+14}_{-14}	$0.07^{+0.09}_{-0.05}$	–
EGS-z11-R0 ¹⁴	11.45	$-19.78^{+0.17}_{-0.17}$	$-0.68^{+0.30}_{-0.30}$	$3.86^{+0.76}_{-0.76}$	$8.64^{+0.32}_{-0.32}$	< 280	$0.90^{+0.28}_{-0.28}$	–
GS-z11-0 ⁷	11.58	$-19.34^{+0.05}_{-0.05}$	$-2.18^{+0.09}_{-0.09}$	$2.20^{+0.28}_{-0.22}$	$8.67^{+0.08}_{-0.13}$	77^{+8}_{-8}	$0.18^{+0.06}_{-0.06}$	$-1.87^{+0.28}_{-0.18}$
GHZ ¹⁵	12.34	$-20.49^{+0.01}_{-0.01}$	$-2.39^{+0.07}_{-0.07}$	$5.20^{+1.10}_{-0.60}$	$9.05^{+0.10}_{-0.25}$	105^{+9}_{-9}	$0.04^{+0.07}_{-0.03}$	$-1.40^{+0.27}_{-0.24}$
UNCOVER-z12 ¹⁶	12.39	$-19.20^{+0.50}_{-0.50}$	$-2.34^{+0.30}_{-0.30}$	$2.15^{+0.81}_{-0.46}$	$8.35^{+0.14}_{-0.18}$	426^{+40}_{-42}	$0.19^{+0.17}_{-0.10}$	$-1.34^{+0.60}_{-0.42}$
GS-z12-0 ⁷	12.63	$-18.23^{+0.16}_{-0.16}$	$-1.84^{+0.19}_{-0.19}$	$1.80^{+0.66}_{-0.43}$	$7.64^{+0.52}_{-0.39}$	144^{+15}_{-15}	$0.19^{+0.17}_{-0.10}$	$-1.44^{+0.23}_{-0.22}$
GS-z13-1-LA ¹⁷	13.01	$-18.49^{+0.04}_{-0.04}$	$-2.75^{+0.10}_{-0.10}$	$0.16^{+0.48}_{-0.15}$	$7.74^{+0.52}_{-0.18}$	14^{+14}_{-7}	$0.04^{+0.05}_{-0.03}$	$-2.52^{+0.57}_{-0.48}$
UNCOVER-z13 ¹⁶	13.08	$-19.40^{+1.80}_{-1.80}$	$-2.59^{+0.20}_{-0.20}$	$1.28^{+0.27}_{-0.18}$	$8.13^{+0.11}_{-0.15}$	309^{+110}_{-74}	$0.04^{+0.08}_{-0.03}$	$-1.57^{+0.35}_{-0.28}$
GS-z13-0 ⁷	13.20	$-18.73^{+0.06}_{-0.06}$	$-2.37^{+0.12}_{-0.12}$	$1.36^{+0.31}_{-0.23}$	$7.95^{+0.19}_{-0.29}$	< 52	$0.04^{+0.08}_{-0.03}$	$-1.69^{+0.28}_{-0.31}$
PAN-z14-1 ¹	13.53	$-20.60^{+0.20}_{-0.20}$	$-2.26^{+0.08}_{-0.08}$	$4.80^{+13.00}_{-4.80}$	$8.23^{+1.14}_{-0.21}$	233^{+10}_{-10}	$0.06^{+0.18}_{-0.30}$	$-1.40^{+1.21}_{-0.60}$
GS-z14-1 ¹⁸	13.90	$-19.00^{+0.40}_{-0.40}$	$-2.71^{+0.19}_{-0.19}$	$2.00^{+0.70}_{-0.40}$	$8.00^{+0.40}_{-0.30}$	< 160	$0.20^{+0.11}_{-0.07}$	$-1.10^{+0.60}_{-0.50}$
GS-z14-0 ¹⁸	14.18	$-20.81^{+0.16}_{-0.16}$	$-2.20^{+0.07}_{-0.07}$	$19.00^{+6.00}_{-6.00}$	$8.84^{+0.09}_{-0.10}$	260^{+2}_{-2}	$0.31^{+0.14}_{-0.17}$	$-0.78^{+0.03}_{-0.03}$
MoM-z14 ¹⁹	14.44	$-20.20^{+0.00}_{-0.00}$	$-2.47^{+0.17}_{-0.17}$	$13.00^{+3.70}_{-3.50}$	$8.10^{+0.30}_{-0.20}$	74^{+15}_{-12}	$0.20^{+0.20}_{-0.10}$	$-1.38^{+0.65}_{-0.56}$

Legend: ¹Donnan et al. (2026), ²Álvarez-Márquez et al. (2026), ³Harikane et al. (2024), ⁴Hsiao et al. (2023), ⁵Marques-Chaves et al. (2026), ⁶Tang et al. (2026), ⁷Curtis-Lake et al. (2023), ⁸Kokorev et al. (2025), ⁹Bunker et al. (2023), ¹⁰Roberts-Borsani et al. (2025), ¹¹Harikane et al. (2026), ¹²Scholtz et al. (2025), ¹³Finkelstein et al. (2024), ¹⁴Rodighiero et al. (2026), ¹⁵Castellano et al. (2024), ¹⁶Wang et al. (2023), ¹⁷Witstok et al. (2025), ¹⁸Carniani et al. (2024), ¹⁹Naidu et al. (2025).

$m < m_0$ ($m \geq m_0$) live forever (die immediately). Thus, for simplicity, we set $(1-R) \approx 1$ for numerical estimates. As all the other quantities are known, we use eq. 5 and the observed value of M_* for each galaxy to derive Δ_{t_*} .

2.4. Specific star formation rate

Armed with the above expressions for the SFR (eq. 2) and M_* (eq. 5), it is straightforward to write the specific star formation rate, $\text{sSFR} = \text{SFR}/M_*$, as

$$\text{sSFR} = 0.64 \frac{(1+z)^{3/2}}{(1-R)\Delta_{t_*}} \text{Gyr}^{-1}. \quad (6)$$

We note that the sSFR is a function of redshift only and grows monotonically. This trend, with $\Delta_{t_*} \approx 1$, reproduces well the available data and existing models (for a detailed comparison see Ferrara 2024a; Santini et al. 2025).

2.5. Super-Eddington condition

The basic idea behind AFM is that galaxies can go through evolutionary phases in which their bolometric

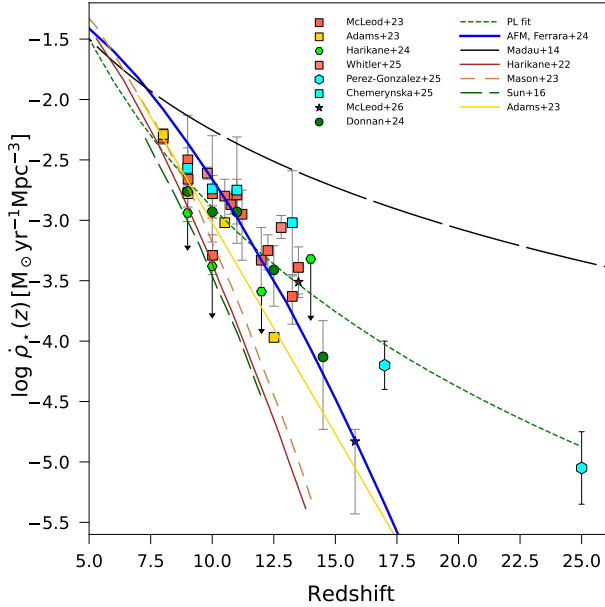


Figure 3. The comoving star formation rate density evolution predicted by AFM (blue line) is compared with available data and other models (lines) in the literature. Data are taken from McLeod et al. (2023); Adams et al. (2024); Harikane et al. (2024); Whittler et al. (2023); Pérez-González et al. (2025); Chemerynska et al. (2024); Madau & Dickinson (2014); Harikane et al. (2022); Mason et al. (2023); Sun & Furlanetto (2016); Adams et al. (2023); Donnan et al. (2024); McLeod et al. (2026). Also shown is a power-law fit (green line) to the data.

luminosity, L_{bol} , becomes super-Eddington,

$$L_{\text{bol}} > L_E^{\text{eff}} = A^{-1} L_E, \quad (7)$$

where $L_E = (4\pi G m_p c / \sigma_T) M_* = 1.26 \times 10^{38} (M_*/M_\odot) \text{ erg s}^{-1}$ is the classical Eddington luminosity. This is reduced by a “boost” factor $A \approx \sigma_d / \sigma_T$, i.e. the ratio of the dust-to-Thomson cross-section in a dusty medium. Nakazato & Ferrara (2024) find that

$$A \simeq 1800 \left(\frac{Z}{Z_\odot} \right) \left[1 + \frac{N_{\text{H}}}{10^{23.5} \text{ cm}^{-2}} \right]^{-1}, \quad (8)$$

where Z is the gas metallicity (solar value $Z_\odot = 0.0142$ Asplund et al. 2009) and N_{H} the hydrogen column density in the galaxy. For simplicity, we will neglect the weak N_{H} dependence.

As L_{bol} is proportional to the SFR and $L_E \propto M_*$, Ferrara (2024a) showed that the super-Eddington condition eq. 7 translates into one on the sSFR:

$$\text{sSFR} > \text{sSFR}^* \simeq 1.4 \left(\frac{Z_\odot}{Z} \right) \left(\frac{2}{f_{\text{bol}}} \right) \text{ Gyr}^{-1}, \quad (9)$$

where $f_{\text{bol}} \simeq 2$ is the bolometric to UV correction (Fiore et al. 2023), and we have used eq. 8 to eliminate A .

Eq. 9 represents the necessary condition for a galaxy to develop a radiation-driven outflow displacing its dust and gas to larger radii.

The gas metallicity, i.e. the metal-to-gas mass ratio $Z = M_Z/M_g$, can be estimated from the IMF-averaged SN metal yield $y_Z = 2.41 M_\odot$. Following Ferrara et al. (2025c) this can be written in closed form as

$$Z \simeq y_Z \nu \frac{(1-R)}{a(z, \epsilon_*)}. \quad (10)$$

The previous expression also accounts for the cosmological accretion via the term

$$a(z, \epsilon_*) = 6.23 [-a_0 - a_1(1+z)] \left(\frac{0.01}{\epsilon_*} \right); \quad (11)$$

where (a_0, a_1) are parameters that depend on cosmology, and the linear matter power spectrum. These are provided³ in Appendix C of Correa et al. (2015).

Combining eqs. 9 and 10 leads to conclude that *on average* galaxies (using fiducial values of the parameters) become super-Eddington for the first time when the star formation efficiency satisfies the inequality

$$\epsilon_*(v_c) \gtrsim 0.04 \Delta_{t_*} (1+z)^{-1/2}. \quad (12)$$

2.6. Dust obscuration

Having established when the galaxy enters the super-Eddington phase, we now aim at determining if and when the galaxy will become obscured during its evolution. As star formation proceeds, supernovae (SN) will inject freshly synthesized dust grains which attenuate the stellar light. Finally $\xi_d = M_d/M_* = y_d \nu / (1-R)$ is the production-only⁴ dust-to-stellar mass ratio. We follow Ferrara et al. (2025c) and take $y_d = 0.1 M_\odot$ for the SN dust yield. The dust optical depth at 1500\AA can be written as

$$\tau_{\text{UV}} = \frac{\kappa_{\text{UV}} \xi_d}{2\pi q r_e^2} M_*, \quad (13)$$

where r_e and M_* are given by eq. 1 and eq. 5, respectively; $q = (1, 2)$ for (disk, spherical) geometry⁵, $\kappa_{\text{UV}} = 1.26 \times 10^5 \text{ cm}^2 \text{ g}^{-1}$ and $\tau_{\text{UV}} = 2.655 \tau_V$ are the dust mass absorption coefficient for a Milky Way extinction curve (Weingartner & Draine 2001). The factor

³ For reference, when averaged over $8 < \log(M_0/M_\odot) < 14$, $(a_0, a_1) = (0.25, -0.75)$.

⁴ As we are interested in redshift $z > 10$ the timescale for the destruction processes tend to be larger than the Hubble time and can be neglected to a first approximation.

⁵ To conservatively minimize the optical depth we assume $q = 2$, also consistent with the quasi-spherical stellar shape of super-early simulated galaxies (Kohandel et al. 2025).

Table 2. Predicted properties of super-early galaxies. Galaxies are coded as G1 to G17 (see legend below).

Property	G1	G2	G3	G4	G5	G6	G7	G8	G9	G10	G11	G12	G13	G14	G15	G16	G17
z	9.94	10.05	10.10	10.56	10.70	10.80	10.92	11.01	11.04	11.44	11.45	12.39	12.63	13.08	13.53	13.90	14.18
r_e [pc]	170	293	520	420	524	555	636	560	453	340	280	426	144	309	233	160	260
λ	0.0057	0.0259	0.0354	0.0237	0.0431	0.0491	0.0505	0.0274	0.0324	0.0343	0.0248	0.0478	0.0172	0.0417	0.0249	0.0214	0.0218
v_c [km s $^{-1}$]	344.14	131.72	171.97	220.35	153.98	145.19	164.28	269.63	184.83	137.74	156.87	138.43	133.32	124.08	164.43	136.32	223.07
ϵ_*	0.0458	0.0119	0.0185	0.0269	0.0155	0.0140	0.0172	0.0350	0.0207	0.0128	0.0160	0.0129	0.0121	0.0107	0.0172	0.0126	0.0273
Δt_*	0.18	2.35	1.27	0.28	3.02	3.67	5.03	0.31	3.66	4.23	3.18	3.27	0.78	3.57	1.26	1.84	1.38
r_{out}/r_e	4.77	7.40	3.24	1.68	8.63	9.25	9.64	1.24	14.55	24.47	4.93	6.70	3.53	22.15	8.14	7.30	5.63
$\nu_f = \delta/\sigma$	5.11	3.46	3.84	4.39	3.84	3.79	4.00	4.93	4.22	3.87	4.07	4.12	4.13	4.13	4.70	4.47	5.48
$\log(M/M_\odot)$	11.843	10.585	10.930	11.226	10.751	10.669	10.824	11.464	10.971	10.566	10.735	10.525	10.464	10.350	10.696	10.435	11.065
$\log(M_*/M_\odot)$	8.950	8.230	8.500	8.300	8.620	8.580	8.960	8.700	9.050	8.500	8.640	8.350	7.640	8.130	8.230	8.000	8.840
SFR [$M_\odot \text{ yr}^{-1}$]	117.00	1.70	5.90	18.00	3.54	2.69	4.78	43.00	8.20	2.10	3.86	2.15	1.80	1.28	4.80	2.00	19.00
ssSFR [Gyr^{-1}]	131.28	10.01	18.66	90.21	8.49	7.08	5.24	85.80	7.31	6.64	8.84	9.60	41.24	9.49	28.26	20.00	27.46
ssSFR* [Gyr^{-1}]	6.28	24.48	15.77	11.34	19.92	22.17	18.26	9.05	15.32	25.60	20.59	27.37	29.74	34.86	22.34	31.35	14.74
A_{UV}	1.832	0.503	0.358	0.753	0.284	0.333	0.642	1.562	0.309	0.182	1.803	0.479	0.479	0.105	0.157	0.503	0.753
A_V	0.920	0.200	0.140	0.310	0.110	0.130	0.260	0.740	0.120	0.070	0.900	0.190	0.190	0.040	0.060	0.200	0.310
β	-1.243	-2.258	-2.343	-2.103	-2.385	-2.357	-2.173	-1.497	-2.371	-2.441	-1.271	-2.272	-2.272	-2.484	-2.455	-2.258	-2.103
$M_{\text{UV}}^{\text{int}}$	-23.690	-19.096	-20.447	-21.658	-19.893	-19.594	-20.219	-22.604	-20.805	-19.326	-19.986	-19.351	-19.158	-18.788	-20.223	-19.273	-21.717
$M_{\text{UV}}^{\text{int}}$	-21.859	-18.594	-20.089	-20.905	-19.609	-19.261	-19.577	-21.042	-20.496	-19.143	-18.183	-18.872	-18.679	-18.683	-20.066	-18.770	-20.963
Z [Z_\odot]	0.2230	0.0572	0.0888	0.1235	0.0703	0.0632	0.0767	0.1548	0.0914	0.0547	0.0680	0.0511	0.0471	0.0402	0.0627	0.0447	0.0950
$\log(n_M/\text{Mpc}^{-3})$	-7.14	-3.06	-3.94	-5.13	-3.78	-3.61	-4.09	-6.39	-4.60	-3.65	-4.13	-4.02	-3.97	-3.86	-5.22	-4.56	-7.22

Legend (galaxy codes to original names):

- G1 = EGS-25297 G2 = UNCOVER-26185 G3 = CEERS2-7929 G4 = CAPERS.UDS-z10 G5 = EGS-22637
- G6 = M_0M -z11-2 G7 = M_0M -z11-1 G8 = CAPERS.UDS-z11 G9 = CEERS2-588 G10 = MAISIE
- G11 = EGS-z11-R0 G12 = UNCOVER-z12 G13 = GS-z12-0 G14 = UNCOVER-z13 G15 = PAN-z14-1
- G16 = GS-z14-1 G17 = GS-z14-0

2.655 accounts for the differential attenuation between 1500Å and the V-band for the adopted extinction curve.

When the super-Eddington condition $\text{sSFR} > \text{sSFR}^*$ condition is satisfied, a radiation-driven outflow develops. The dust and the gas, initially contained within r_e are then displaced to a larger radius, $r_{\text{out}} > r_e$. In this case, we replace r_e with r_{out} in the previous formula to compute τ_{UV} . Finally, the V-band attenuation is computed from

$$A_V = -2.5 \log \frac{1 - e^{-\tau_V}}{\tau_V}, \quad (14)$$

as appropriate for a disk configuration in which stars and dust are intermixed (Ferrara et al. 2022). The observed (i.e. including dust attenuation) galaxy AB magnitude at 1500 Å is obtained from the following expression:

$$M_{\text{UV}} = 5.89 - 2.5 \log(\mathcal{K}_{1500} \text{SFR}) + A_{\text{UV}}, \quad (15)$$

where the SFR-luminosity conversion factor $\mathcal{K}_{1500} = 0.587 \times 10^{10} L_{\odot} / (M_{\odot} \text{yr}^{-1})$, following Ferrara (2024a); A_{UV} is computed from eq. 14 using the above relation between UV and visual optical depth.

From the attenuation, A_V , we can also predict the value of the spectral UV slope β . Such conversion is uncertain as it depends on the properties of the dust, which are poorly understood at these very early epochs. We take an empirical approach, and adopt the best-fit to the observed data, i.e.

$$\beta = -2.54 + 1.41 A_V. \quad (16)$$

In summary, we use four observed quantities $r_e, \text{SFR}, M_*, A_V$ as constraints to the AFM, which returns the predicted values of additional 12 properties for each galaxy. Among these, three are also generally observed, and can be directly compared with the model. These are the attenuated UV magnitude, M_{UV} , the UV slope, β , the metallicity, Z . The other nine are measured only in a limited number of objects and/or cannot be experimentally determined. These are $\lambda, v_c, \epsilon_*, \Delta_{t_*}, r_{\text{out}}, M, \nu_{\delta}, \text{sSFR}^*, M_{\text{UV}}^{\text{int}}$ (the unattenuated UV magnitude), and n_M which are then used to test the outflow-based AFM scenario and its implications for the evolution of super-early galaxies.

3. RESULTS

We apply the AFM model described above to the spectroscopically confirmed sample of 32 $z > 10$ galaxies whose observed properties are listed in Tab. 1. For all of them the redshift, UV magnitude, UV spectral slope, star formation rate and stellar mass are available. Instead, for the effective radius in many cases only upper limits are given. Finally, for some systems A_V and metallicity data are unconstrained.

First, we will discuss the general properties of the sample, and then outline the emerging evolutionary scenario for these systems. As already mentioned, we initially restrict our analysis to the “extended” subset of super-early galaxies, i.e. those showing a measured effective radius $r_e > 150$ pc. However, we will return to the “compact” objects in Sec. 4.

3.1. Physical properties

The predicted properties of the 17 extended super-early galaxies in the sample are summarized in Fig. 4, where they are ordered in increasing redshift sequence. We show six quantities: the instantaneous star formation efficiency, spin parameter, halo mass, stellar age, outflow outer radius in units of the effective radius, and metallicity (bottom right). These quantities are not yet directly observable (metallicity is a partial exception).

In each panel we also highlight whether the galaxy is super-Eddington (and therefore potentially able to launch an outflow), and whether it is obscured. We adopt $A_V = 0.5$, corresponding to $\tau_V \simeq 1$, as the threshold between the transparent and obscured regime. Additional predictions not shown here can be found in Tab. 2. In the following we discuss the results and their implications separately for each quantity.

3.1.1. Star formation efficiency

The first notable finding is that the star formation efficiency is moderate, ranging from $0.01 < \epsilon_* < 0.045$ with a median value of 0.016. These results are in excellent agreement with those shown in Fig. 3 of Harikane et al. (2026), who find that $\epsilon_* < 0.03$ for all super-early galaxies, with the only exception of CEERS2-588, which appears to have a somewhat higher efficiency ($\epsilon_* \simeq 0.1$) compared to our prediction for the same system ($\epsilon_* = 0.02$).

We note, though, that Harikane et al. (2026) obtain ϵ_* assuming a fixed halo mass $\log(M/M_{\odot}) = 10.7$ (the most massive halo in the CEERS survey volume, and in perfect agreement with the median M value found here; see Sec. 3.1.3), while for CEERS2-588 we derive a slightly larger value $M = 10^{10.97} M_{\odot}$. Adopting our value for the halo mass, the observed efficiency would drop to $\epsilon_* = 0.054$, which is in better – though not yet perfect – agreement with our result.

Finally, we note that the values inferred by Harikane et al. (2026) refer to the *integrated* star formation efficiency (i.e., the gas-to-star conversion efficiency) rather than the *instantaneous* efficiency we use here. This difference may also contribute to the discrepancy.

No significant variations with redshift are seen. However, we note that the two red, super-Eddington galaxies (EGS-25297 and CAPERS_UDS_z11) lie $2\text{--}3\sigma$ away

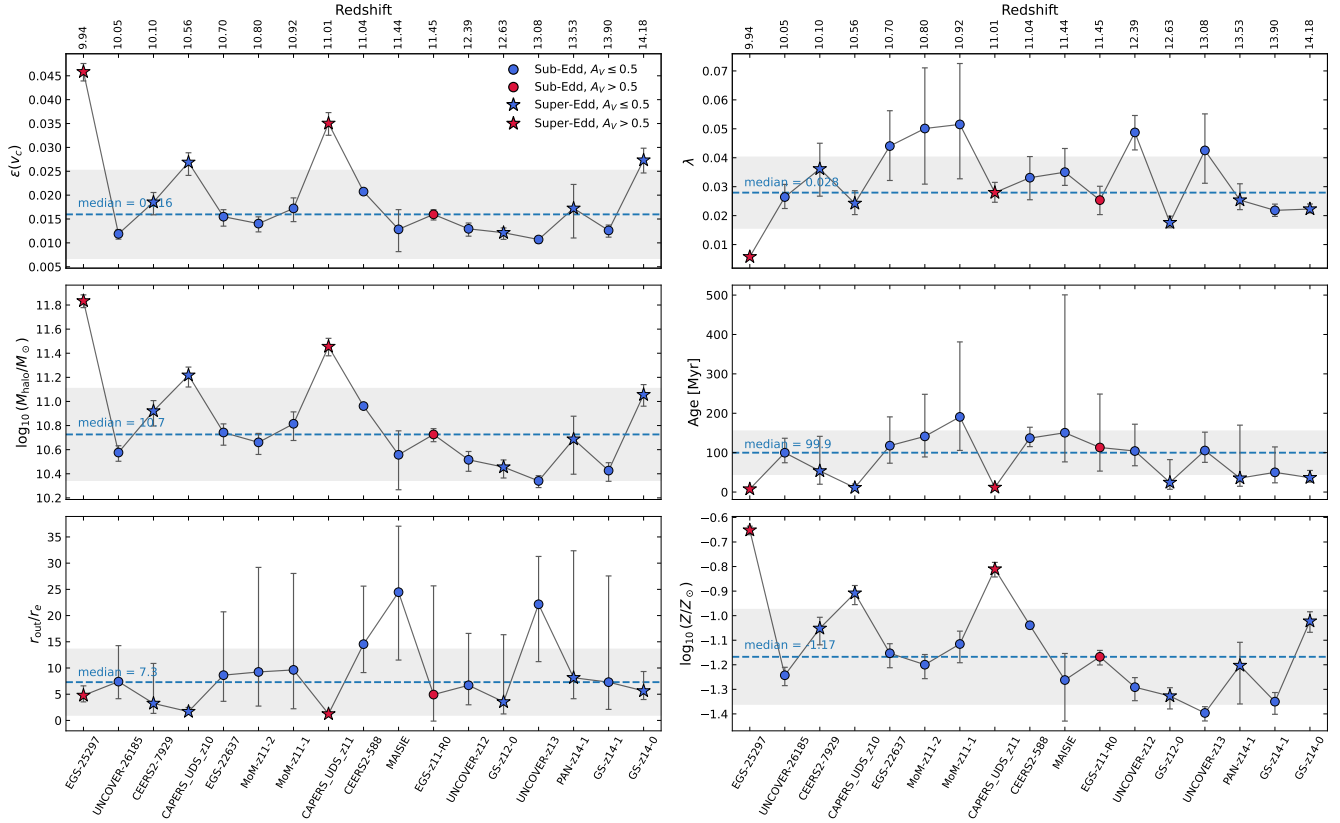


Figure 4. Properties of super-early galaxies predicted by AFM. For the 17 extended galaxies (ordered according to their redshift, shown on the top axis) in the sample we show the instantaneous star formation efficiency (top left panel), spin parameter (top right), halo mass (middle left), stellar age (middle right), outflow outer radius in units of the effective radius (bottom left), metallicity (bottom right). Data points are labelled with different markers/colors according to their Eddington parameter and visual attenuation (see legend). The horizontal line (bue dashed) shows the median of the sample, with the grey area spanning the 16th-84th percentile range.

from the median value. In Sec. 3.2 we will interpret this evidence in the framework of an evolutionary scenario.

3.1.2. Spin parameter

The second notable finding concerns the halo spin parameter λ . Our inferred values span a range $0.006 < \lambda < 0.05$ with a median of $\lambda = 0.028$. These values are consistent with typical spin parameters predicted for dark matter halos in cosmological simulations, which peak around $\lambda \simeq 0.03 - 0.04$ (Bullock et al. 2001; Macciò et al. 2007; Dutton & Macciò 2014; Angel et al. 2016), and show no significant trend with redshift, as also found here.

Again, an exception to this trend is provided by EGS-25297, which shows a lower spin parameter, $\lambda \approx 0.006$, lying more than 2σ below the median value. Low-spin haloes are characterised by deeper potential wells and more concentrated mass distributions, which may hinder the launching of large-scale outflows and allow dust to remain in the galaxy centre, thereby producing the redder colours observed in these systems. This inter-

pretation is consistent with the evolutionary scenario outlined in Sec. 3.2.

3.1.3. Halo mass

AFM predicts that Blue Monsters are hosted by relatively massive halos, with masses spanning almost one order of magnitude, $10.3 < \log M < 11.2$, and a median value $\log M = 10.7$. These halos represent $\simeq 4\sigma$ fluctuations of the density field; the rarest 5.5σ peak is represented by GS-z14-0 ($z = 14.18$). We also see a hint of decreasing halo mass towards high redshifts.

Red monsters in a super-Eddington phase like EGS-25297 and CAPERS_UDS_z11 live instead on even more massive halos with $\log M \gtrsim 11.5$. Interestingly, the newly discovered $z = 11.45$ Red Monster EGS-z11-R0 is instead in a sub-Eddington phase and its halo mass is the median one. Later on, we will see that this galaxy is on a similar evolutionary path as the other two Red Monsters, but it is seen at an earlier evolutionary phase.

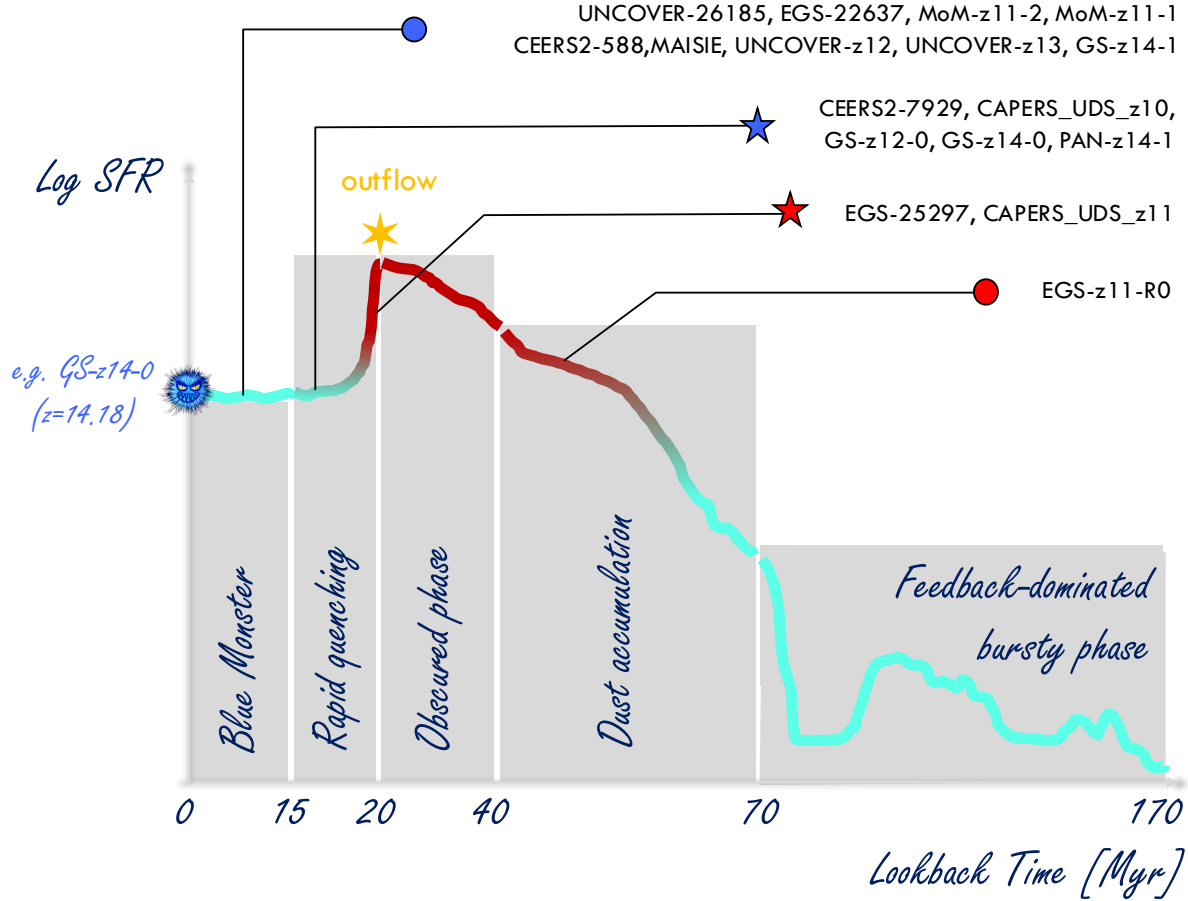


Figure 5. Sketch of the possible evolutionary path leading to the formation of a Blue Monster in the Attenuation-Free Model (AFM), based on the detailed study of GS-z14-0 at $z = 14.18$ presented in Ferrara (2024b). The values of the lookback time and of the SFR are only indicative, as they depend on the properties of individual galaxies, as discussed in the text.

3.1.4. *Stellar ages*

Our predictions on the stellar ages are presented in the middle right panel of Fig. 4. There is considerable galaxy-to-galaxy scatter in this quantity, ranging from $\simeq 10$ Myr (e.g. CAPERS_UDS_z10) to $\simeq 190$ Myr (MoM-z11-1). Such a large age implies that this galaxy started to form stars as early as $z = 16.6$. Ages do not seem to decrease with redshift, although out of the five most distant galaxies, four are more than 1σ below the median value of 99.9 Myr.

Interestingly, the two super-Eddington Red Monsters are characterised by very young stellar ages ≈ 10 Myr. As we have seen above, they live in very massive halos in which star formation is accelerated by the vast availability of gas and the deep potential well.

3.1.5. *Outflow radius*

One of the key features of AFM is that it predicts that super-early galaxies, due to their compactness and astounding UV luminosity, can drive powerful radiative outflows displacing the dust and gas up to a radius r_{out} significantly larger than the effective radius r_e . The ratio of these quantities for the galaxies in the sample is shown in the bottom left panel of Fig. 4.

On average, Blue Monsters have been able to push the dust to $7.3 r_e$, thus decreasing the dust optical depth (see Eq. 13). Some of the outflows are still ongoing (those in galaxies that are still in the super-Eddington phase). These systems tend to have smaller outflow radii as the outflow has not fully developed yet. Among the systems in this phase are GS-z12-0 and GS-z14-0 (see blue stars in the panel).

Other Blue Monsters are instead sub-Eddington, and the outflow has run out of power, reaching an almost stalling configuration. These are characterised by the

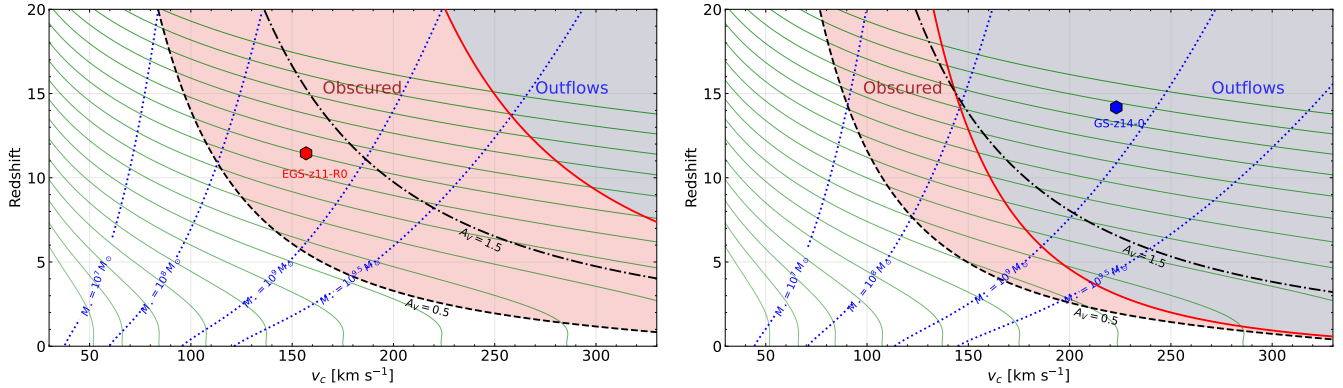


Figure 6. Evolutionary path of super-early galaxies shown in the redshift - circular velocity (proxy for halo mass) plane. The green lines (bottom to top) are the tracks of galaxies whose star formation activity starts at $z_* = 9, 10, \dots, 25$, respectively. Also shown are stellar mass isocountours (blue dotted). As the circular velocity, halo and stellar mass increase with time the galaxy accumulates dust and becomes redder, crossing the $A_V = 0.5$ (dashed) line representing our definition of “obscured” systems; for reference we also plot the $A_V = 1.5$ (dot-dashed) curve. When the track crosses the sSFR^* threshold (red line) the galaxy becomes super-Eddington, and launches an outflow, eventually displacing the dust and turning it into a Blue Monster. *Left panel:* Case for the Red Monster EGS-z1-R0 ($z = 11.45$). *Right:* Same for the Blue Monster GS-z14-0 ($z = 14.18$).

largest r_{out}/r_e values, such as e.g. Maisie ($z = 11.44$) and other galaxies (blue circles).

Finally, as expected in our scenario, Red Monsters are still in the dust accumulation phase or have just entered the super-Eddington one. Hence their outflows are still absent or have limited size (e.g., CAPERS_UDS_z11).

3.1.6. Metallicity

The last quantity we scrutinise is the metallicity. Typically, Blue Monsters show significant metallicities (median $\log(Z/Z_\odot) = -1.17$), although there is a scatter of about 0.2 dex around that value. Galaxies at $z < 11$ lie close to or above the median, while those at higher redshifts are instead well below such value. This indicates a redshift trend, which is generally expected.

The relatively high metallicity values are consistent with a relatively extended evolution (as we have seen, the ages are of order 100 Myr on average). As we have already alluded to, a Blue Monster likely emerges from a past Red Monster phase; this process requires time. Red monsters living in massive halos are still embedded in the dust cocoon; they are young, and the dust and metals they produce are retained. For this reason they have higher metallicity. Strikingly, a Red Monster like EGS-25297 is predicted by AFM to have $\log(Z/Z_\odot) = -0.65$, a value not too discrepant from the one derived from SED fitting by Donnan et al. (2026), $\log(Z/Z_\odot) = -1.0^{+0.08}_{-0.08}$.

3.2. Evolutionary scenario

The question that naturally arises from the above analysis of the predicted super-early galaxy properties is whether their apparent diversity can be reconciled with

a common evolutionary path. In other words, can we identify the leading physical processes that give rise to blue (and red) monsters?

To answer this question, we take advantage of the detailed study (Ferrara 2024b) of a representative Blue Monster, GS-z14-0 at $z = 14.18$, whose observed and predicted properties are listed in Tab. 1 and Tab. 2, respectively. In that work the observed properties and spectrum of GS-z14-0 were obtained using a physical model of its star formation history (SFH), which we use here as a template to propose a possible common evolutionary path of super-early galaxies. A schematic view of the SFH as a function of lookback time, t_L , from the observed epoch is presented in Fig. 5. Its main features are summarized below.

Star formation activity is largely suppressed by molecular cooling dissociation in “minihalos”, i.e. halos with virial temperature $T_{\text{vir}} \leq 10^4$ K (see e.g. Ciardi & Ferrara 2005). Hence, stars begin to form at $z = z_*$, corresponding to $\simeq 170$ Myr, when growing halos cross that boundary ($M_0 \simeq 10^8 M_\odot$) and $\text{Ly}\alpha$ cooling becomes efficient. The halo mass growth with redshift can be obtained by time-integrating the cosmological accretion of matter. A handy fit to $M(z)$ is provided by Correa et al. (2015):

$$M(z) = M_0 \left(\frac{1+z}{1+z_0} \right)^{a_0} e^{a_1(z-z_0)}, \quad (17)$$

where a_0 and a_1 are introduced in eq. 11. Following a very bursty and intermittent initial phase, star formation becomes more continuous as the galaxy grows in stellar mass. As a result, dust produced by SNe continues to accumulate, increasingly attenuating

the galaxy’s light, eventually completely obscuring the galaxy. As the SFR continues to increase, sustained by vigorous mass accretion (see eq. 11), the increased dust/metal content lowers the value of the critical specific star formation, sSFR^* , and the galaxy becomes super-Eddington and launches a powerful outflow. The outflow very rapidly (on a timescale of a few Myr) displaces the dust and gas to a radius $r_{\text{out}} > r_e$, as we have seen in the previous Section. The outflow also quenches the SFR due to the decreased availability of gas. At that point, the sSFR falls below sSFR^* and eventually the outflow radius approaches its observed value. This is found (Sec. 3.1.5) to be on average $r_{\text{out}}/r_e \approx 7$, which implies outflows extending to \approx kpc scales.

This evolutionary path is schematically illustrated by Fig. 5. Also shown, based on the analysis performed in Sec. 3 above, are the locations of EGS-z11-R0 (left panel) and GS-z14-0 (right). The comparison highlights the different evolutionary paths and phases of Red vs. Blue Monsters. According to AFM, the $z > 10$ Red Monsters are observed either in the dust accumulation phase or immediately after they become super-Eddington, when the outflow starts to clear the dust cocoon. In between, we predict the existence of a possibly brief phase of complete obscuration in which the galaxies are too faint and red to be seen by JWST (i.e., JWST-dark galaxies), with the possible exception of some MIRI bands. A detailed modeling of this phase (SED, number counts) is deferred to further study.

Blue Monsters first appear at the end of the rapid quenching phase, when the outflow is still ongoing but gradually running out of power. Observationally, evidence of quenching in CEERS2-588 from MIRI spectra has been reported by Harikane et al. (2026), in line with the present results. They remain blue and bright even when the outflow stalls at r_{out} and the galaxy settles into a more moderate SFR. The proposed evolution also explains why extended Blue Monsters show almost featureless spectra and weak emission lines, consistent with the post-starburst scenario we propose here.

In principle, a blue phase can also occur at large look-back times, i.e., earlier during the evolution and at the beginning of the dust accumulation phase. Although the SFR – and hence the UV luminosity – is probably too low for the galaxy to be detected, this evolutionary phase might be within reach of lensing experiments, such as the GLIMPSE survey (Atek et al. 2025). It would be interesting in the future to use the AFM to make detailed predictions concerning this phase.

To further corroborate the above evolutionary scenario, in Fig. 6 we plot the evolutionary tracks (green lines) of galaxies starting to form stars at different red-

shifts in the range $9 < z_* < 25$. The tracks are shown in the redshift–circular velocity plane (proxy for halo mass); the stellar mass isocontours (blue dotted) allow us to infer M_* along the track. In both panels, we show for reference the curves for $A_V = 0.5$ (our working definition of a red/obscuRed Monster) and $A_V = 1.5$. These curves refer to pre-outflow values; as the outflow displaces the dust, A_V decreases to a much lower value, as clarified when discussing Fig. 4. The location of the red curve is set by the Eddington condition $\text{sSFR} = \text{sSFR}^*$ (Eq. 12). We note that both the A_V and the critical sSFR curves depend on the galaxy properties, such as λ and Δ_{t_*} , and therefore vary from galaxy to galaxy.

To illustrate our point, in Fig. 6 we compare a Red Monster (EGS-z11-R0) with a Blue Monster (GS-z14-0). As expected, EGS-z11-R0, with its inferred $v_c = 156.87 \text{ km s}^{-1}$, is located well into the obscured region ($A_V = 0.9$), into which it entered at $z = 13.5$, having started to form stars at $z_* \simeq 20$. Our model predicts that EGS-z11-R0 will continue to accumulate dust and become severely attenuated for a long time (up to $z \simeq 7.5$), when it will have reached $v_c = 320 \text{ km s}^{-1}$ corresponding to a halo mass $\log M = 11.95$. At that point, the outflow starts clearing the dust. Strikingly, this halo mass is comparable to that inferred for the other $z = 9.94$ Red Monster EGS-25297, which is in the super-Eddington phase. We caution, however, that if the accumulation phase lasts for a long time, allowing the galaxy to become very large, our assumption of a central, compact source driving the outflow might no longer be satisfied. A firm conclusion on this issue requires further work.

The situation is dramatically different for GS-z14-0 ($z = 14.18$), which is instead actively powering an outflow whose current outer radius is $r_{\text{out}} \approx 5 \times r_e = 1.3 \text{ kpc}$. This system started to form stars at $z_* \simeq 24$ and passed through a relatively brief obscured phase lasting from $z = 19.2$ to 16.6 , or 45 Myr. As the galaxy’s $\text{sSFR} \approx 2 \times \text{sSFR}^*$ (Table 2), the outflow is still ongoing, sustained by a significant SFR of $19 M_\odot \text{ yr}^{-1}$. Interestingly, Carniani et al. (2026) report evidence for CIII] $\lambda\lambda 1907, 1909$ line emission from the outflowing material at least up to a radius $\gtrsim 400 \text{ pc}$. From the spectra they also set an upper limit to the star formation efficiency $\epsilon_* < 0.08$, which aligns well with the value found here ($\epsilon_* = 0.0273$).

In summary, the above scenario, highlighting the key role played by radiation-driven outflows in the early universe, provides a coherent interpretation framework to understand the diversity of super-early galaxies and their evolutionary properties, while making testable

and specific predictions for ongoing high-redshift galaxy searches.

4. COMPACT GALAXIES SUBSET

So far we have concentrated on the analysis of the extended-galaxy subset of our sample. However, from Table 1 we see that 12 galaxies have measured or upper-limit values of $r_e < 150$ pc. Explaining such extremely compact structure is very challenging within the framework of our model. A practical example involving the prototypical compact galaxy GHZ2 ($r_e = 105 \pm 9$ pc) clarifies the difficulty.

The very small size of GHZ2 requires a slowly rotating halo, with $\lambda = 0.0097$ – a value corresponding to a 2.3σ deviation from the mean. In addition, the highly compact structure together with the large stellar mass would make the galaxy extremely obscured (see eq. 13). To decrease A_V to the observed value of ~ 0.04 , the outflow radius would need to be $r_{\text{out}} \approx 23.6$ kpc, i.e., 2.5 times larger than the virial radius of GHZ2 (9.5 kpc). However, according to eq. 12, GHZ2 should not have reached the outflow phase so far. This contradiction suggests that compact galaxies have a different nature from the “normal”, extended population.

Taken together with the presence of strong high-ionization emission lines, and in particular NIV λ 1486 (Harikane et al. 2026), a more plausible explanation is that the emission from compact super-early galaxies is instead dominated by an AGN. Indeed, AGN activity in compact galaxies such as GN-z11 and GHZ2, based on the detection of high-ionization emission lines, has been reported (Maiolino et al. 2024; Castellano et al. 2024). In this case, the galaxy rest-frame UV continuum must be dominated by emission from an AGN accretion disk. Importantly, the presence of the AGN in compact systems would strongly affect the properties inferred from the observations, thus making them rather uncertain.

To quantify the above statement, we proceed as follows. Let us suppose that compact super-early galaxies host a central AGN whose UV luminosity $L_{\text{AGN}} = xL_{\text{UV}}$, where L_{UV} is the galaxy luminosity; further assume that the galaxy light follows a Sercic profile with $n = 1$, i.e. exponential, with length scale $r_s = r_e/1.678$. Then the fraction of the host galaxy light outside a radius r is

$$f_{\text{out}}(r) = e^{-r/r_s} \left(1 + \frac{r}{r_s} \right) \quad (18)$$

If the PSF dominates within a radius $r_0 \approx 1$ FWHM, the host luminosity outside that radius is $L_{\text{UV,out}} = L_{\text{UV}} f_{\text{out}}(r_0)$. Hence, the galaxy *cannot* be detected if

$$\frac{L_{\text{UV,out}}}{L_{\text{AGN}}} = \frac{1}{x} f_{\text{out}}(r_0) < \epsilon_{\text{PSF}}, \quad (19)$$

where $\epsilon_{\text{PSF}} \approx 0.05$ is the fractional PSF-subtraction floor at r_0 . Quantitatively, we fix $r_e = 400$ pc, an average value for the extended-galaxy subset, and hence $r_s = 238$ pc, or $0.06''$ at $z = 11$. To estimate r_0 , we note that for JWST/NIRCam the PSF FWHM is approximately diffraction-limited, $\text{FWHM} \sim \lambda/D$, and for F444W it is of order $0.15''$. From the above expressions, we then find $x = 5.7$, which implies in terms of the host fraction of the total light

$$\frac{L_{\text{UV}}}{L_{\text{tot}}} = \frac{1}{1+x} = 0.15. \quad (20)$$

In conclusion, if the AGN light exceeds 85% of the total, the source is seen as a point source. We consider this occurrence as the most likely explanation of the compact-galaxy subset properties.

5. SUMMARY

In this work, we have investigated the physical origin of the diversity observed among spectroscopically confirmed super-early galaxies at $z > 10$ within the framework of the Attenuation-Free Model (AFM). By applying the model to a sample of 32 galaxies, and focusing on the subset of extended systems, we have derived a coherent set of physical properties — including halo mass, star formation efficiency, metallicity, and outflow characteristics — that are otherwise difficult to constrain observationally. The AFM successfully reproduces the observed UV luminosities, spectral slopes, and attenuation properties, while naturally explaining the coexistence of extremely blue and significantly reddened systems at cosmic dawn.

Our analysis supports an evolutionary scenario in which super-early galaxies undergo a sequence of phases regulated by the interplay between star formation, dust production, and radiation-driven feedback. Galaxies initially build up dust through supernova enrichment, entering an obscured “Red Monster” phase characterized by significant attenuation and moderate-to-high metallicity. As the star formation rate increases, galaxies can reach a super-Eddington regime, triggering powerful radiation-driven outflows that displace dust and gas to kiloparsec scales. This process rapidly reduces the effective optical depth, giving rise to the observed population of bright, UV-transparent “Blue Monsters”. Within this framework, sources such as EGS-z11-R0 are naturally interpreted as systems caught during the dust-enshrouded phase preceding the emergence of blue galaxies.

Overall, the AFM provides a unified physical picture that connects the observed properties of super-early galaxies to their underlying evolutionary paths. It highlights the central role of radiation pressure and outflows

in shaping early galaxy evolution, and makes specific, testable predictions regarding dust distribution, metallicity, and the existence of heavily obscured, potentially JWST-dark progenitors. These results have important implications for our understanding of early star formation, chemical enrichment, and the buildup of the first luminous structures in the Universe.

- The AFM successfully reproduces the observed UV luminosities, spectral slopes, and attenuation properties of $z > 10$ galaxies, supporting a scenario in which dust is present but redistributed by radiation-driven outflows.
- Super-early galaxies exhibit moderate star formation efficiencies ($0.01 \lesssim \epsilon_* \lesssim 0.05$) and reside in massive halos ($\log M/M_\odot \sim 10.7$), corresponding to rare ($\sim 4\text{--}5\sigma$) peaks of the density field.
- Radiation-driven outflows are a ubiquitous and key ingredient of early galaxy evolution, displacing dust to radii $\sim 5\text{--}10 r_e$ and enabling the transition from dust-obscured to UV-bright phases.
- The observed diversity between red and blue galaxies is naturally explained as different evolutionary stages: Red Monsters correspond to dust-rich, pre- or early-outflow phases, while Blue Monsters are systems in which outflows have already reduced the effective attenuation.

- Compact ($r_e \lesssim 150$ pc) systems are difficult to reconcile within the AFM framework. We speculate that their emission is dominated ($> 85\%$) by an AGN component, indicating a distinct physical origin from the extended galaxy population.

Future progress will crucially rely on larger samples and deeper observations with *JWST* and ALMA, which will be essential to test these predictions, constrain the dust and gas distribution in super-early galaxies, and clarify the physical processes driving their rapid evolution at cosmic dawn.

ACKNOWLEDGMENTS

We thank H. Atek, T. Bakx, L. Bisigello, M. Castellano, R. Ellis, C. Kobayashi, M. Llerena, R. Maiolino, D. McLeod, I. Mitsuhashi, T. Morishita, Y. Nakazato, L. Napolitano, L. Pentericci, P. Pérez-González, G. Roberts-Borsani, P. Santini, R. Somerville, M. Stiavelli, S. Tacchella, M. Tang, and J. Zavala for valuable discussions and/or sharing galaxy data. A special thank from AF (he knows why) to M. Ouchi. This work is supported by the ERC Advanced Grant INTERSTELLAR H2020/740120 (PI: Ferrara), and in part by grant NSF PHY-2309135 to the Kavli Institute for Theoretical Physics. This work was started while AF was a Distinguished Visitor at the Institute of Astronomy, Cambridge University, whose generous support and hospitality are kindly acknowledged.

REFERENCES

- Adams, N. J., Conselice, C. J., Ferreira, L., et al. 2023, *MNRAS*, 518, 4755, doi: [10.1093/mnras/stac3347](https://doi.org/10.1093/mnras/stac3347)
- Adams, N. J., Conselice, C. J., Austin, D., et al. 2024, *ApJ*, 965, 169, doi: [10.3847/1538-4357/ad2a7b](https://doi.org/10.3847/1538-4357/ad2a7b)
- Álvarez-Márquez, J., Colina, L., Crespo-Gomez, A., et al. 2026, arXiv e-prints, arXiv:2602.02323, doi: [10.48550/arXiv.2602.02323](https://doi.org/10.48550/arXiv.2602.02323)
- Angel, P. W., Poole, G. B., Ludlow, A. D., et al. 2016, *MNRAS*, 459, 2106, doi: [10.1093/mnras/stw737](https://doi.org/10.1093/mnras/stw737)
- Asplund, M., Grevesse, N., Sauval, A. J., & Scott, P. 2009, *Annual Review of Astronomy and Astrophysics*, 47, 481–522, doi: [10.1146/annurev.astro.46.060407.145222](https://doi.org/10.1146/annurev.astro.46.060407.145222)
- Atek, H., Chisholm, J., Kokorev, V., et al. 2025, arXiv e-prints, arXiv:2511.07542, doi: [10.48550/arXiv.2511.07542](https://doi.org/10.48550/arXiv.2511.07542)
- Austin, D., Conselice, C. J., Adams, N. J., et al. 2024, arXiv e-prints, arXiv:2404.10751, doi: [10.48550/arXiv.2404.10751](https://doi.org/10.48550/arXiv.2404.10751)
- Bouwens, R. J., Stefanon, M., Brammer, G., et al. 2022, arXiv e-prints, arXiv:2211.02607, doi: [10.48550/arXiv.2211.02607](https://doi.org/10.48550/arXiv.2211.02607)
- Bullock, J. S., Dekel, A., Kolatt, T. S., et al. 2001, *ApJ*, 555, 240, doi: [10.1086/321477](https://doi.org/10.1086/321477)
- Bunker, A. J., Saxena, A., Cameron, A. J., et al. 2023, arXiv e-prints, arXiv:2302.07256, doi: [10.48550/arXiv.2302.07256](https://doi.org/10.48550/arXiv.2302.07256)
- Carniani, S., Hainline, K., D’Eugenio, F., et al. 2024, *Nature*, 633, 318, doi: [10.1038/s41586-024-07860-9](https://doi.org/10.1038/s41586-024-07860-9)
- Carniani, S., Jakobsen, P., Venturi, G., et al. 2026, Intense and extended CIII] emission suggests a strong outflow in JADES-GS-z14-0. <https://arxiv.org/abs/2604.11899>
- Casey, C. M., Akins, H. B., Shuntov, M., et al. 2023, arXiv e-prints, arXiv:2308.10932, doi: [10.48550/arXiv.2308.10932](https://doi.org/10.48550/arXiv.2308.10932)
- Castellano, M., Fontana, A., Treu, T., et al. 2023, *ApJL*, 948, L14, doi: [10.3847/2041-8213/accea5](https://doi.org/10.3847/2041-8213/accea5)

- Castellano, M., Napolitano, L., Fontana, A., et al. 2024, arXiv e-prints, arXiv:2403.10238, doi: [10.48550/arXiv.2403.10238](https://doi.org/10.48550/arXiv.2403.10238)
- Castellano, M., Fontana, A., Merlin, E., et al. 2025, *A&A*, 704, A158, doi: [10.1051/0004-6361/202555082](https://doi.org/10.1051/0004-6361/202555082)
- Chemerynska, I., Atek, H., Furtak, L. J., et al. 2024, *MNRAS*, 531, 2615, doi: [10.1093/mnras/stae1260](https://doi.org/10.1093/mnras/stae1260)
- Ciardi, B., & Ferrara, A. 2005, *SSRv*, 116, 625, doi: [10.1007/s11214-005-3592-0](https://doi.org/10.1007/s11214-005-3592-0)
- Correa, C. A., Wyithe, J. S. B., Schaye, J., & Duffy, A. R. 2015, *MNRAS*, 450, 1521, doi: [10.1093/mnras/stv697](https://doi.org/10.1093/mnras/stv697)
- Cullen, F., McLeod, D. J., McLure, R. J., et al. 2024, *MNRAS*, 531, 997, doi: [10.1093/mnras/stae1211](https://doi.org/10.1093/mnras/stae1211)
- Curtis-Lake, E., Carniani, S., Cameron, A., et al. 2023, *Nature Astronomy*, doi: [10.1038/s41550-023-01918-w](https://doi.org/10.1038/s41550-023-01918-w)
- Dayal, P., & Ferrara, A. 2018, *PhR*, 780, 1, doi: [10.1016/j.physrep.2018.10.002](https://doi.org/10.1016/j.physrep.2018.10.002)
- Dayal, P., Ferrara, A., Sommovigo, L., et al. 2022, *MNRAS*, 512, 989, doi: [10.1093/mnras/stac537](https://doi.org/10.1093/mnras/stac537)
- Dekel, A., Sarkar, K. C., Birnboim, Y., Mandelker, N., & Li, Z. 2023, *MNRAS*, 523, 3201, doi: [10.1093/mnras/stad1557](https://doi.org/10.1093/mnras/stad1557)
- Donnan, C. T., McLure, R. J., Dunlop, J. S., et al. 2024, arXiv e-prints, arXiv:2403.03171, doi: [10.48550/arXiv.2403.03171](https://doi.org/10.48550/arXiv.2403.03171)
- Donnan, C. T., McLeod, D. J., McLure, R. J., et al. 2026, arXiv e-prints, arXiv:2601.11515, doi: [10.48550/arXiv.2601.11515](https://doi.org/10.48550/arXiv.2601.11515)
- Dottorini, D., Calabrò, A., Pentericci, L., et al. 2024, arXiv e-prints, arXiv:2412.01623, doi: [10.48550/arXiv.2412.01623](https://doi.org/10.48550/arXiv.2412.01623)
- Dutton, A. A., & Macciò, A. V. 2014, *MNRAS*, 441, 3359, doi: [10.1093/mnras/stu742](https://doi.org/10.1093/mnras/stu742)
- Ferrara, A. 2024a, *A&A*, 684, A207, doi: [10.1051/0004-6361/202348321](https://doi.org/10.1051/0004-6361/202348321)
- . 2024b, *A&A*, 689, A310, doi: [10.1051/0004-6361/202450944](https://doi.org/10.1051/0004-6361/202450944)
- Ferrara, A., Carniani, S., di Mascia, F., et al. 2025a, *A&A*, 694, A215, doi: [10.1051/0004-6361/202452368](https://doi.org/10.1051/0004-6361/202452368)
- Ferrara, A., Giavalisco, M., Pentericci, L., et al. 2025b, *The Open Journal of Astrophysics*, 8, 125, doi: [10.33232/001c.143600](https://doi.org/10.33232/001c.143600)
- Ferrara, A., Pallottini, A., & Dayal, P. 2023, *MNRAS*, 522, 3986, doi: [10.1093/mnras/stad1095](https://doi.org/10.1093/mnras/stad1095)
- Ferrara, A., Pallottini, A., & Sommovigo, L. 2025c, *A&A*, 694, A286, doi: [10.1051/0004-6361/202452707](https://doi.org/10.1051/0004-6361/202452707)
- Ferrara, A., Sommovigo, L., Dayal, P., et al. 2022, *MNRAS*, 512, 58, doi: [10.1093/mnras/stac460](https://doi.org/10.1093/mnras/stac460)
- Finkelstein, S. L., Leung, G. C. K., Bagley, M. B., et al. 2023, arXiv e-prints, arXiv:2311.04279, doi: [10.48550/arXiv.2311.04279](https://doi.org/10.48550/arXiv.2311.04279)
- . 2024, *ApJL*, 969, L2, doi: [10.3847/2041-8213/ad4495](https://doi.org/10.3847/2041-8213/ad4495)
- Fiore, F., Ferrara, A., Bischetti, M., Feruglio, C., & Travascio, A. 2023, *ApJL*, 943, L27, doi: [10.3847/2041-8213/acb5f2](https://doi.org/10.3847/2041-8213/acb5f2)
- Harikane, Y., Nakajima, K., Ouchi, M., et al. 2024, *ApJ*, 960, 56, doi: [10.3847/1538-4357/ad0b7e](https://doi.org/10.3847/1538-4357/ad0b7e)
- Harikane, Y., Ono, Y., Ouchi, M., et al. 2022, *ApJS*, 259, 20, doi: [10.3847/1538-4365/ac3dfc](https://doi.org/10.3847/1538-4365/ac3dfc)
- Harikane, Y., Ouchi, M., Oguri, M., et al. 2023, *ApJS*, 265, 5, doi: [10.3847/1538-4365/acaaa9](https://doi.org/10.3847/1538-4365/acaaa9)
- Harikane, Y., Inoue, A. K., Ellis, R. S., et al. 2025, *ApJ*, 980, 138, doi: [10.3847/1538-4357/ad9b2c](https://doi.org/10.3847/1538-4357/ad9b2c)
- Harikane, Y., Perez-Gonzalez, P. G., Alvarez-Marquez, J., et al. 2026, arXiv e-prints, arXiv:2601.21833, doi: [10.48550/arXiv.2601.21833](https://doi.org/10.48550/arXiv.2601.21833)
- Hsiao, T. Y.-Y., Abdurro'uf, Coe, D., et al. 2023, arXiv e-prints, arXiv:2305.03042, doi: [10.48550/arXiv.2305.03042](https://doi.org/10.48550/arXiv.2305.03042)
- Katz, H., Cameron, A. J., Saxena, A., et al. 2025, *The Open Journal of Astrophysics*, 8, 104, doi: [10.33232/001c.142570](https://doi.org/10.33232/001c.142570)
- Kohandel, M., Pallottini, A., & Ferrara, A. 2025, *A&A*, 704, A39, doi: [10.1051/0004-6361/202555499](https://doi.org/10.1051/0004-6361/202555499)
- Kokorev, V., Chávez Ortiz, Ó. A., Taylor, A. J., et al. 2025, arXiv e-prints, arXiv:2504.12504, doi: [10.48550/arXiv.2504.12504](https://doi.org/10.48550/arXiv.2504.12504)
- Leung, G. C. K., Bagley, M. B., Finkelstein, S. L., et al. 2023, *ApJL*, 954, L46, doi: [10.3847/2041-8213/acf365](https://doi.org/10.3847/2041-8213/acf365)
- Li, Z., Dekel, A., Sarkar, K. C., et al. 2023, arXiv e-prints, arXiv:2311.14662, doi: [10.48550/arXiv.2311.14662](https://doi.org/10.48550/arXiv.2311.14662)
- Liu, B., & Bromm, V. 2023, arXiv e-prints, arXiv:2312.04085, doi: [10.48550/arXiv.2312.04085](https://doi.org/10.48550/arXiv.2312.04085)
- López-Corredoira, M., & Gutiérrez, C. M. 2026, *MNRAS*, doi: [10.1093/mnras/stag089](https://doi.org/10.1093/mnras/stag089)
- Macciò, A. V., Dutton, A. A., van den Bosch, F. C., et al. 2007, *MNRAS*, 378, 55, doi: [10.1111/j.1365-2966.2007.11720.x](https://doi.org/10.1111/j.1365-2966.2007.11720.x)
- Madau, P., & Dickinson, M. 2014, *ARA&A*, 52, 415, doi: [10.1146/annurev-astro-081811-125615](https://doi.org/10.1146/annurev-astro-081811-125615)
- Maiolino, R., Scholtz, J., Witstok, J., et al. 2024, *Nature*, 627, 59, doi: [10.1038/s41586-024-07052-5](https://doi.org/10.1038/s41586-024-07052-5)
- Marques-Chaves, R., Álvarez-Márquez, J., Colina, L., et al. 2026, arXiv e-prints, arXiv:2602.02322, doi: [10.48550/arXiv.2602.02322](https://doi.org/10.48550/arXiv.2602.02322)
- Mason, C. A., Trenti, M., & Treu, T. 2023, *MNRAS*, 521, 497, doi: [10.1093/mnras/stad035](https://doi.org/10.1093/mnras/stad035)

- Matteri, A., Ferrara, A., & Pallottini, A. 2025, arXiv e-prints, arXiv:2503.18850, doi: [10.48550/arXiv.2503.18850](https://doi.org/10.48550/arXiv.2503.18850)
- McLeod, D. J., Donnan, C. T., McLure, R. J., et al. 2023, arXiv e-prints, arXiv:2304.14469, doi: [10.48550/arXiv.2304.14469](https://doi.org/10.48550/arXiv.2304.14469)
- McLeod, D. J., Dunlop, J. S., McLure, R. J., et al. 2026, A search for the first galaxies across $> 0.6 \text{ deg}^2$ of JWST imaging: new evidence for a rapid decline in star-formation activity at $z > 12$. <https://arxiv.org/abs/2604.16666>
- Mitsuhashi, I., Suess, K. A., Leja, J., et al. 2025, arXiv e-prints, arXiv:2510.13240, doi: [10.48550/arXiv.2510.13240](https://doi.org/10.48550/arXiv.2510.13240)
- Mo, H., van den Bosch, F. C., & White, S. 2010, *Galaxy Formation and Evolution*, doi: [10.1017/CBO9780511807244](https://doi.org/10.1017/CBO9780511807244)
- Morales, A. M., Finkelstein, S. L., Leung, G. C. K., et al. 2024, *The Astrophysical Journal Letters*, 964, L24, doi: [10.3847/2041-8213/ad2de4](https://doi.org/10.3847/2041-8213/ad2de4)
- Morishita, T., Stiavelli, M., Chary, R.-R., et al. 2024, *ApJ*, 963, 9, doi: [10.3847/1538-4357/ad1404](https://doi.org/10.3847/1538-4357/ad1404)
- Naidu, R. P., Oesch, P. A., van Dokkum, P., et al. 2022, Two Remarkably Luminous Galaxy Candidates at $z \approx 11 - 13$ Revealed by JWST, arXiv, doi: [10.48550/ARXIV.2207.09434](https://doi.org/10.48550/ARXIV.2207.09434)
- Naidu, R. P., Oesch, P. A., Brammer, G., et al. 2025, arXiv e-prints, arXiv:2505.11263, doi: [10.48550/arXiv.2505.11263](https://doi.org/10.48550/arXiv.2505.11263)
- Nakazato, Y., Ceverino, D., & Yoshida, N. 2024, *ApJ*, 975, 238, doi: [10.3847/1538-4357/ad7d0b](https://doi.org/10.3847/1538-4357/ad7d0b)
- Nakazato, Y., & Ferrara, A. 2024, arXiv e-prints, arXiv:2412.07598, doi: [10.48550/arXiv.2412.07598](https://doi.org/10.48550/arXiv.2412.07598)
- Napolitano, L., Castellano, M., Pentericci, L., et al. 2025, *ApJ*, 989, 75, doi: [10.3847/1538-4357/ade706](https://doi.org/10.3847/1538-4357/ade706)
- Pérez-González, P. G., Östlin, G., Costantin, L., et al. 2025, arXiv e-prints, arXiv:2503.15594, doi: [10.48550/arXiv.2503.15594](https://doi.org/10.48550/arXiv.2503.15594)
- Planck Collaboration, Ade, P. A. R., Aghanim, N., et al. 2014, *A&A*, 571, A16, doi: [10.1051/0004-6361/201321591](https://doi.org/10.1051/0004-6361/201321591)
- Pérez-González, P. G., Costantin, L., Langeroodi, D., et al. 2023, Life beyond 30: probing the $-20 < M_{UV} < -17$ luminosity function at $8 < z < 13$ with the NIRCam parallel field of the MIRI Deep Survey. <https://arxiv.org/abs/2302.02429>
- Roberts-Borsani, G., Oesch, P., Ellis, R., et al. 2025, arXiv e-prints, arXiv:2508.21708, doi: [10.48550/arXiv.2508.21708](https://doi.org/10.48550/arXiv.2508.21708)
- Robertson, B., Johnson, B. D., Tacchella, S., et al. 2024, *ApJ*, 970, 31, doi: [10.3847/1538-4357/ad463d](https://doi.org/10.3847/1538-4357/ad463d)
- Rodighiero, G., Bisigello, L., Iani, E., et al. 2023, *MNRAS*, 518, L19, doi: [10.1093/mnras/slac115](https://doi.org/10.1093/mnras/slac115)
- Rodighiero, G., Ferrara, A., Catone, M., et al. 2026, arXiv e-prints, arXiv:2603.15841, doi: [10.48550/arXiv.2603.15841](https://doi.org/10.48550/arXiv.2603.15841)
- Santini, P., Castellano, M., Calabrò, A., et al. 2025, arXiv e-prints, arXiv:2512.09139, doi: [10.48550/arXiv.2512.09139](https://doi.org/10.48550/arXiv.2512.09139)
- Saxena, A., Cameron, A. J., Katz, H., et al. 2024, arXiv e-prints, arXiv:2411.14532, doi: [10.48550/arXiv.2411.14532](https://doi.org/10.48550/arXiv.2411.14532)
- Scholtz, J., Maiolino, R., D'Eugenio, F., et al. 2025, *A&A*, 697, A175, doi: [10.1051/0004-6361/202348804](https://doi.org/10.1051/0004-6361/202348804)
- Semenov, V. A. 2026, arXiv e-prints, arXiv:2602.04950, doi: [10.48550/arXiv.2602.04950](https://doi.org/10.48550/arXiv.2602.04950)
- Shibuya, T., Ouchi, M., & Harikane, Y. 2015, *ApJS*, 219, 15, doi: [10.1088/0067-0049/219/2/15](https://doi.org/10.1088/0067-0049/219/2/15)
- Somerville, R. S., & Davé, R. 2015, *ARA&A*, 53, 51, doi: [10.1146/annurev-astro-082812-140951](https://doi.org/10.1146/annurev-astro-082812-140951)
- Somerville, R. S., Yung, L. Y. A., Lancaster, L., et al. 2025, *MNRAS*, 544, 3774, doi: [10.1093/mnras/staf1824](https://doi.org/10.1093/mnras/staf1824)
- Sommovigo, L., Ferrara, A., Pallottini, A., et al. 2022, *MNRAS*, 513, 3122, doi: [10.1093/mnras/stac302](https://doi.org/10.1093/mnras/stac302)
- Sun, G., & Furlanetto, S. R. 2016, *MNRAS*, 460, 417, doi: [10.1093/mnras/stw980](https://doi.org/10.1093/mnras/stw980)
- Tang, M., Stark, D. P., Mason, C. A., et al. 2026, *ApJ*, 1001, 38, doi: [10.3847/1538-4357/ae4edb](https://doi.org/10.3847/1538-4357/ae4edb)
- Tang, M., Stark, D. P., Plat, A., et al. 2025, *ApJ*, 991, 217, doi: [10.3847/1538-4357/adfd57](https://doi.org/10.3847/1538-4357/adfd57)
- Tripodi, R., Napolitano, L., Pentericci, L., et al. 2026, arXiv e-prints, arXiv:2603.06409, doi: [10.48550/arXiv.2603.06409](https://doi.org/10.48550/arXiv.2603.06409)
- Wang, B., Fujimoto, S., Labbé, I., et al. 2023, *The Astrophysical Journal Letters*, 957, L34, doi: [10.3847/2041-8213/acef07](https://doi.org/10.3847/2041-8213/acef07)
- Weingartner, J. C., & Draine, B. T. 2001, *ApJ*, 548, 296, doi: [10.1086/318651](https://doi.org/10.1086/318651)
- Whitler, L., Endsley, R., Stark, D. P., et al. 2023, *MNRAS*, 519, 157, doi: [10.1093/mnras/stac3535](https://doi.org/10.1093/mnras/stac3535)
- Willott, C. J., Desprez, G., Asada, Y., et al. 2024, *ApJ*, 966, 74, doi: [10.3847/1538-4357/ad35bc](https://doi.org/10.3847/1538-4357/ad35bc)
- Witstok, J., Jakobsen, P., Maiolino, R., et al. 2025, *Nature*, 639, 897, doi: [10.1038/s41586-025-08779-5](https://doi.org/10.1038/s41586-025-08779-5)
- Ziparo, F., Ferrara, A., Sommovigo, L., & Kohandel, M. 2023, *MNRAS*, 520, 2445, doi: [10.1093/mnras/stad125](https://doi.org/10.1093/mnras/stad125)